Lognormal firing rate distribution reveals prominent fluctuation–driven regime in spinal motor networks

Peter C. Petersen[1] ***and Rune W. Berg***[1]*

[1] *Faculty of Health and Medical Sciences, Department of Neuroscience and Pharmacology, University of Copenhagen, Blegdamsvej 3, 24.3.47, DK-2200 Copenhagen N, Denmark*

∗*Correspondence: runeb@sund.ku.dk*

ABSTRACT

When spinal circuits generate rhythmic movements it is important that the neuronal activity remains within stable bounds to avoid saturation and to preserve responsiveness. In what dynamical regime does the neuronal population operate in order to achieve this? Here, we simultaneously record from hundreds of neurons in lumbar spinal circuits and establish the neuronal fraction that operates within either a 'mean-driven' or a 'fluctuation–driven' regime during generation of multiple motor behaviors. We find a rich diversity of firing rates across the neuronal population as reflected in a lognormal distribution and demonstrate that half of the neurons spend at least 50% of the time in the 'fluctuation–driven' regime regardless of behavior. Since neurons in this regime have a 'supralinear' input–output curve, which enhances sensitivity, whereas the mean–driven regime reduces sensitivity, this fraction may reflect a fine trade–off between stability and sensitivity in order to maintain flexibility across motor behaviors.

INTRODUCTION

Rhythmic movements, such as walking, running, scratching and breathing, consist of a recurrent sequence of activity, which is generated by large circuits primarily in the spinal cord. Although, this sequential activity is formed by collective communication among spinal neurons, it is unknown how the participation is shared versus divided within the population. Do all neurons, which participate in a given motor activity, spike at approximately the same rate? Or do only some neurons spike at high rate, while most others spike at lower rates? An arrangement with a spectrum of different firing rates could be beneficial by adding the possibility of increasing the overall activity, for instance during uphill walking where a stronger force is needed. In this way the spinal circuit could enhance flexibility by adopting a diversity of firing rates across the population. Other networks in the central nervous system face a similar challenge of how to distribute the activity across the population in order to collectively increase the dynamic range [Wohrer *et al.*, 2013]. In sensory processing, neural circuits must be able to retain sensitivity both to weak and strong input. Weak stimuli are amplified whereas strong stimuli are attenuated in order to reduce saturation. If there is too much activity, the circuit reaches saturation and therefore loses the ability to resolve differences in sensory input. Furthermore, amplification of weak signals by recurrent excitation pose the risk of unstable activity, which can spin out of control [Vogels *et al.*, 2005]. This computational challenge of how networks maintain both stability and sensitivity is an open question especially for spinal networks.

Stability has primarily been investigated in cortical networks and much evidence suggest that local excitation is carefully balanced by inhibition to assure stability and to widen the range of operation [Galarreta

and Hestrin, 1998; Shu *et al.*, 2003]. It is well–established that unstable states such as epileptiform activity can easily be achieved by shifting the balance in favor of excitation, e.g. by blocking inhibition [Bazhenov *et al.*, 2008; Dichter and Ayala, 1987]. The concept of *balanced excitation (E) and inhibition (I)* (balanced networks in short) was introduced two decades ago [Shadlen and Newsome, 1994; van Vreeswijk and Sompolinsky, 1996] and has sparked numerous studies both theoretical [Amit and Brunel, 1997; Kumar *et al.*, 2008; Ozeki *et al.*, 2009; van Vreeswijk and Sompolinsky, 1998] as well as experimental [Berg *et al.*, 2007; Higley and Contreras, 2006; Kishore *et al.*, 2014; Okun and Lampl, 2008; Wehr and Zador, 2003]. The primary purpose of theoretical models of balanced networks was initially to understand irregular spiking, which was widely observed in experiments [Bell *et al.*, 1995; Shadlen and Newsome, 1994]. Irregular spiking was puzzling because it could not be explained by random arrival of excitatory input alone, since this randomness was effectively regularized by temporal integration [Softky and Koch, 1993]. Models of balanced networks not only were able to explain irregular spiking, but also explained other interesting phenomena, such as emergent linearity [van Vreeswijk and Sompolinsky, 1996] and self–sustained stable network activity [Amit and Brunel, 1997; Hansel and Mato, 2001; Ikegaya *et al.*, 2013].

The consensus view thus became that irregular spiking results from a mean membrane potential, which is lurking just below threshold, where it is restrained by inhibition concurrent with excitation [Bell *et al.*, 1995; Salinas and Sejnowski, 2000; Shadlen and Newsome, 1998], although synchrony of random excitation is sometimes needed when individual synaptic potentials are small [Stevens and Zador, 1998]. This view was essentially predicted much earlier in random walk models [Gerstein and Mandelbrot, 1964]. In this subthreshold domain the spikes are evoked by synaptic transients and therefore belong to the *fluctuation–driven regime* [Kuhn *et al.*, 2004; Tiesinga *et al.*, 2000]. This is in contrast to the more traditional *mean–driven* spiking (**Figure 1**), where the mean membrane potential (V_m) is well above threshold and spike timing is controlled by after–hyperpolarization [Gerstner *et al.*, 2014; Renart *et al.*, 2007]. These two regimes have contrasting manifestations (**Table 1**): The fluctuation–driven regime has a skewed/lognormal firing rate distribution whereas the mean–driven regime has regular spiking and a symmetric distribution. A simple mechanism has been proposed to explain the lognormal firing in the fluctuation–driven regime by Roxin *et al.* [2011]: The skewness in distribution arises out of a *supralinear* transformation of the synaptic input, which is Gaussian by virtue of the central limit theorem (**Figure 1A**). A response to multiple input, which is larger than the sum of their individual responses (i.e. *supralinear*), will enhance sensitivity [Rubin *et al.*, 2015] and therefore this mechanism may constitute an important physiological purpose.

This is in contrast to the mean–driven regime where the summation is linear or even *sublinear*, which will transform a normally distributed input to a normally (as opposed to lognormally) distributed firing rate (**Figure 1B**). Such linear (or sublinear) transformation will reduce rather than enhance sensitivity and therefore the mean–driven regime will curb network activity [Ahmadian *et al.*, 2013]. These two transformations may work together into an S-shaped IO-curve, where weak input are amplified yet the network is kept stable for strong activity (**Figure 1C**). Sample neurons in the two regimes are shown (**Figure 1D-E**). If this mechanism is true, then the shape of the firing rate distribution will reveal the spiking regime of a given neuron. The degree to which neurons operate in one versus the other regime may hold the key to understanding stability, dynamic range and other important properties of network operations. Yet this still remains to be investigated, especially in spinal networks.

Here, we investigate the regimes of operation of spinal neurons during different rhythmic motor behaviors, which are generated in the lumbar spinal circuits of turtles. We test the theoretical scheme put forward by Roxin *et al.* [2011], by assessing the synaptic input, the spike response function in subthreshold domain, and determine the shape of the firing rate distribution. The mechanical stability of the turtle preparation allows electrophysiological recordings of unprecedented quality, such that we can combine intracellular recording with multi–electrode arrays, and thus determine the fraction of the population in the two regimes at all times. The high resistance to anoxia of turtles allows using adult animals with fully developed spinal circuitry, which have healthy network activity and which can perform multiple complex motor behaviors [Stein, 2005]. Thus, we can investigate the population activity during, not just one behavior, but multiple motor behaviors. Custom designed high–density silicon electrodes recorded the population activity from hundreds of cells in the dorsoventral and rostrocaudal axes along with the intracellular V_m of single neurons and multiple relevant motor nerves (**Figure 2**). This is a unique experimental investigation, because it explores the link between neuronal ensemble data, which in itself is rare in spinal motor research, and the forefront of theoretical neuroscience.

Table 1: Two regimes of neuronal spiking and their definition, properties and causes.

	Fluctuation–driven	**Mean–driven**	**Key references**
Definition	$R_m I_{total} < V_{thres}$	$R_m I_{total} > V_{thres}$	[Brunel, 2000; Gerstner *et al.*, 2014]
Properties	Lower firing rates	Higher firing rates	
	Irregular spiking	Regular spiking	[Amit and Brunel, 1997] [Shadlen and Newsome, 1998] [van Vreeswijk and Sompolinsky, 1998]
	Lognormal/Skewed distribution	Symmetric distribution	[Buzsáki and Mizuseki, 2014] [Mizuseki and Buzsáki, 2013; Roxin *et al.*, 2011]
Cause	Balanced E/I	Intrinsic currents, unbalanced E/I	[Bell *et al.*, 1995; Shadlen and Newsome, 1994; Softky and Koch, 1993]
	Synchronized excitation		[Stevens and Zador, 1998]

RESULTS

The parallel spiking activity of 200–300 single units were recorded in the medial to ventral horns of lumbar spinal segments involved in motor rhythm generation (**Figure 2A**). The location of the electrode arrays in the ventral area of the lumbar enlargement was verified by histology (**Figure 2B-C** and **Figure supplement 1**). The array recordings were performed simultaneously with recording of the intracellular activity of a single neuron in parallel with electroneurograms (ENGs) from relevant motor nerves (**Figure 2D**). Site–specific rhythmic hindlimb scratching was induced by tactile touch of the carapace [Berkowitz *et al.*, 2010; Stein, 2005] and could be reproduced reliably over multiple trials [Petersen *et al.*, 2014; Vestergaard and Berg, 2015]. The extracellular multielectrode arrays, which were used, were custom–designed for the spinal cord (Berg64-probe, Neuronexus inc.) to enable efficient polytrode spike sorting (**Figure 2E** and **Figure supplement 2**). The distribution of spike count firing rates across the population was skewned (**Figure 2F**), but resembled a normal distribution on logarithmic x-axis (inset), i.e. a *lognormal* distribution. This lognormal distribution indicates a wide degree of participation in the motor activity across the population. In the following, we will investigate the participation of neurons within the mean– and fluctuation–driven regimes and how this is linked to the lognormal firing rate distribution, both across the population and within individual cells. We start by addressing the mechanism behind the lognormal firing rate distribution in intracellular recorded data, before addressing the concurrent population activity.

Mechanisms behind lognormal distribution and the fluctuation–regime

Two mechanisms have previously been proposed to explain the skewned lognormal firing rate distribution, which is also observed in other parts of the nervous system [Buzsáki and Mizuseki, 2014]. Lognormal distributions could either arise from a nonlinear transformation of normally distributed inputs [Roxin *et al.*, 2011] (**Figure 1A**) or from a linear transformation of a lognormally distributed synaptic input [Wohrer *et al.*, 2013]. The latter mechanism was considered in connection with the sparse spiking activity in auditory cortex [Hromádka *et al.*, 2008; Koulakov *et al.*, 2009] and since synaptic weights within neocortex have a heavy tail lognormal distribution rather than a Gaussian distribution [Ikegaya *et al.*, 2013; Song *et al.*, 2005]. Models also show that the V_m distribution can be either skewed or Gaussian depending on the synaptic input intensity [Ostojic, 2011]. Therefore, to distinguish between the proposed mechanisms, it is important to first assess whether the synaptic current is normally versus lognormally distributed. Secondly, to test whether the transformation of the synaptic input to spiking output is linear versus supralinear. We started by addressing the first requirement by investigating the synaptic input in intracellular recordings. The most relevant part of the data was found during the peak of a locomotor cycle where the V_m was in vicinity of V_{thres} and was dominated by synaptic potentials (**Figs. 1D** and **3A**). The motor activity was clearly non–stationary, which means that the spike activity was likely to move between the fluctuation– and mean–regime. Nevertheless, the rhythmic activity possessed a separation of timescales in the sense that the activity between cycles (∼1 s) contained much larger excursions in V_m than within cycles (∼2-400 ms). Here, the mean V_m did not change much and for practical purposes it could be considered constant within the cycle. In the following analysis of the intracellular data we regarded the dynamics in V_m as stationary within a cycle – well aware that the comparison to theoretical models, which are based on assumption of stationarity, should be taken with a grain

of salt. We intended to investigate the symmetry of the distribution of synaptic current using this assumption. The synaptic current within a cycle is difficult to assess, but rather than the mean current, we were primarily interested in the fluctuations in current, which we could approximate from V_m via Ohm's law under the following conditions. Within a cycle, the mean V_m was just below threshold and did not change its value much. Therefore the voltage–activated conductances were approximately constant such that there was an Ohmic relationship between synaptic current and V_m. This is likely justified for neurons in fluctuation–driven regime, since the conductance is often high and dominated by balanced E/I synaptic input [Destexhe *et al.*, 2003; Kumar *et al.*, 2008]. The high conductance suppresses the coupling between V_m and intrinsic conductance in a divisive manner [Kolind *et al.*, 2012; Tiesinga *et al.*, 2000]. Thus, in the fluctuation–driven regime the non–Ohmic contributions were likely smaller and the IV_m-relationship more linear than in the mean–driven regime.

Normally distributed synaptic input

We intended to test the hypothesis of normally distributed input, but since the approximation of using the variability in V_m as a proxy for the variability in synaptic current is most valid for the neurons in fluctuation–driven regime, we needed a way to distinguish neurons that were primarily in fluctuation–driven regime. We therefore propose a novel metric, *the return map ratio*, which quantifies the degree of fluctuations leading up to a spike (**Figure 3 supplement 1**). The return map ratio (RMR) quantifies how direct the subthreshold V_m–trajectory is between spikes and this forms the basis for selecting neurons in our analysis (if RMR < 0.7). An RMR close to 0.5 has fluctuation–driven spiking whereas a value close to 1 suggests mean–driven spiking. A sample neuron, which was found in the fluctuation–driven regime based on this metric illustrates how we obtained the distribution of sub–threshold V_m (**Figure 3A**). The distribution was estimated both by selecting the V_m in between spikes (temporal distribution) and by collecting instances of V_m prior to spike peak in a spike triggered overlay ('sigma' in **Figure 3B**). These two estimates are in agreement with one another for the sample cell (**Figure 3C**). This agreement is also found across the population as quantified by the mean and SD (**Figure 3D**). The skewness for the distributions across the population is small and scattered around zero as expected for normal (symmetric) distributions (**Figure 3E**). From these data we conclude that the subthreshold V_m–distributions are not skewed, but rather symmetrical and *Gaussian–like* (cf. inset distributions, **Figure 3E**). Nevertheless, the minimal requirement for confirming the two–regime hypothesis for the single neuron is that the synaptic current (not the synaptic potentials) is Gaussian (**Figure 1**). As we argued earlier, if there is an Ohmic relationship between current and potential, which is likely during high–conductance states, then this requirement would be granted. More importantly, now that we do find a Gaussian V_m–distribution, it is difficult to contemplate a non-linear IV_m-relationship, which would result in such a symmetric distribution. The synaptic input current would have to have a finely matched inverse distribution to cancel out this non–linearity in order to achieve a symmetric V_m–distribution. A more parsimonious explanation therefore is that, since the synaptic potentials are normally distributed, they are a result of a linear transformation of synaptic currents, which are also normally distributed.

So far, we have only looked at V_m–distributions of single neurons, which operate primarily in the subthreshold domain, and found that the synaptic input is most likely normally distributed. We do not know whether the synaptic input is also normally distributed in the mean–driven regime, but since the synaptic input is normally–distributed in the subthreshold region, it is likely also normally–distributed in the suprathreshold region. Otherwise, the input statistics from the presynaptic neurons would have to depend on the threshold of the post–synaptic neuron, which is unlikely.

Mean V_m across the population is normally distributed

Above, we established that the synaptic input to a given neuron is likely normally distributed, and if this input is transformed in a supralinear fashion, the output firing rate distribution will be skewed. Nevertheless, the foundation of the skewness in population rate distribution (**Figure 2F**) is not necessarily directly linked to the skewness of the instantaneous rate distribution of single neurons. In principle, it is possible to have a population with a normal distribution of mean firing rates, where the cells themselves have lognormally distributed firing rates and vice versa. Therefore, we needed to address the distribution of mean V_m across the population and test whether this was skewed or normal. Further, since the sub–threshold IO-curve is

linked to threshold, it is important to establish the distance of mean V_m from threshold with respect to the size of synaptic fluctuations, i.e. standard deviation of V_m (σ). This distribution, i.e. $(V_m - V_{thres})/\sigma$, turns out to also be normally distributed with a mean around 3σ from threshold (**Figure 3 supplement 2**). If we assume, when normalizing V_m this way, the IO-curve has approximately the same nonlinearity across all neurons (**Figure 3E**), the population distribution of firing rates will also be skewed due to the nonlinear transformation of the normally–distributed input (**Figure 3 supplement 1F**) to a lognormally–distributed output. These results are in qualitative accordance with the scheme proposed previously [Roxin *et al.*, 2011]. As another piece of the puzzle, we need to establish the shape of the neuronal response function, which rarely has been done in the subthreshold domain.

Neuronal response–function in subthreshold domain is nonlinear.

The link between a normally distributed input and a lognormally distributed output is a supralinear transformation. To test whether this is a hallmark of the fluctuation–driven regime, we needed to estimate the input–output (IO)–function for the subthreshold domain. The IO–function of neurons is a fundamental property of the nervous system, and therefore it is well-characterized both theoretically [Gerstner *et al.*, 2014] and experimentally [Silver, 2010]. Nevertheless, it has rarely been established for subthreshold spiking. Here, we estimated the IO-function for subthreshold spiking via the probability of eliciting a spike as a function of V_m in the following way. First, we collected instances of V_m shortly before the spike–onset, where V_m is depolarized yet still not part of the deterministic spike trajectory. The probability that a given value of V_m will cause a spike was estimated as the histogram of V_m–instances (gray histogram, **Figure 4A**) divided by the total time spent at all values of V_m (green histogram). This gives the empirical relationship between V_m and the firing rate [Jahn *et al.*, 2011; Vestergaard and Berg, 2015]. The IO–function had a strong non–linear shape (**Figure 4B**). To capture the curvature we fitted both a power–law and an exponential and the curvature had a weak negative correlation with the SD of the V_m–fluctuation (**Figure 4C–D**) as demonstrated previously [Vestergaard and Berg, 2015]. Similar expansive nonlinearity has previously been characterized in sensory–driven neurons [Anderson *et al.*, 2000; Hansel and van Vreeswijk, 2002; Miller and Troyer, 2002]. It will transform the normally–distributed synaptic potentials into a *log–normally*–distributed spiking output in the fluctuation-driven regime (**Figure 1A**). For mean–driven spiking the IO-function is not supralinear, but rather linear (or even sublinear), and the normally–distributed synaptic input will therefore be transformed to a normally distributed spiking output (**Figure 1B**). In conclusion, neurons that have fluctuation–driven spiking also have a non–linear IO-transformation of synaptic potentials to spiking output.

Lognormal firing rate distribution in single neurons

The normally distributed input combined with the nonlinear IO–transformation should result in a skewed lognormal firing rate in the single neuron. To confirm this, we measured the distribution of the instantaneous firing rate, i.e. the inverse of ISIs. The quiet period in between burst cycles were not included in the analysis (**Figure 1D–E**), since in these periods V_m was far from V_{thres} and therefore in an irrelevant part of the IO–function. The firing rate distribution of many cells was positively skewed and resembled a normal distribution with near zero skewness on a log-scale (sample cell shown in **Figure 5A**). This is expected for poisson–like spiking in the fluctuation–driven regime [Ostojic, 2011]. Nevertheless, distributions for all the intracellularly recorded neurons ($n = 68$) were skewed to a varying degree from strong positive to zero skewness on a linear axis and similarly shifted downwards on log axis (cf. gray and green histograms, **Figure 5B**). This suggests that neurons were found in a spectrum between fluctuation– and mean–driven spiking. More negative log–skewness were associated with higher mean rates (**Figure 5C**). This is probably due to a larger presence in the mean–regime at higher firing rates, where the distribution skewness is expected to be negative on a log–scale, i.e. Gaussian on a linear scale. Note that the spectrum of skewness was substantially larger than it was for the V_m distributions above (**Figure 3E**). Skewed Gaussian distributions are shown to illustrate the range of skewness in the data (**Figure 5D**). In conclusion, these results suggest that the skewness in firing rates is an indicator of the degree of participation in the fluctuation–driven regime.

Time spent in regimes: intracellular data

A neuron is not just spiking in either the fluctuation– or the mean–driven regime, rather, it likely spends time in both regimes during motor activity. To estimate the amount of time a given neuron spends in either of the two regimes we calculated the fraction of time that the smoothed V_m was above versus below threshold. We first look at two heuristic neurons, one in the fluctuation–driven regime and one in the mean–driven regime. The fluctuation–driven neuron spent most of the time below threshold (**Figure 6A**) and had more irregular spiking as quantified by a local measure of irregularity, the CV_2 (green line). CV_2 is the difference of two adjacent ISIs divided by their mean [Bruno *et al.*, 2015; Holt *et al.*, 1996]. In contrast, the mean–driven neuron spent most time above threshold and had more regular spiking, i.e. CV_2 closer to zero (**Figure 6B**). Since the threshold was firing rate–dependent due to the inactivation of the Na^+–conductance (**Figure 6 supplement 1**) we used the most hyperpolarized value of threshold (broken line). The distribution of CV_2 for all trials had higher mean for the fluctuation–driven cell than the mean–driven (cf. arrows, **Figure 6C**). Also, the cumulative time spent below threshold was higher for the fluctuation–driven cell (96%) than the mean–driven cell (35%, **Figure 6D**). This fraction of time spent below threshold was quantified for every neuron ($n = 68$) and the population distribution had a strong mode at 1 (top, **Figure 6E**) suggesting many neurons spent much time in the fluctuation–driven regime. To compress the diversity within the population into a simpler representation, we used the reverse cumulative distribution of neurons versus time spent below threshold (bottom, **Figure 6E**). This indicates how many neurons (y-axis) spent at least a given fraction of time (x-axis) below threshold. The intercept with the 50%–line (broken line) indicates what fraction of time half the population at least spent below threshold. This fraction is remarkably high (84%) suggesting a prominent presence within the fluctuation–driven regime.

Transition between regimes by current injection

Mean- and fluctuation-driven spiking can be distinguished by important traits such as degree of irregularity and log-skewness of the firing–rate distribution. To verify these traits, we used another sample neuron as a heuristic illustration. We injected different levels of either positive or negative bias currents in different trials while keeping all else constant. A negative constant current injection (-1.0 nA) caused a decrease in firing rate and a slight increase in irregularity (green line) compared with zero injected current (**Figure 7A–B**). Similarly, a positive current injection (1.7 nA) caused more spikes and a decrease in irregularity (**Figure 7C**) consistent with a movement between regimes (inset in **Figure 7A**). The decrease in irregularity with increasing input was further quantified as a negative correlation between mean CV_2 and injected current ($R = -0.84$, $p \ll 0.001$) over multiple trials (n=18, **Figure 7D**). This is qualitatively in agreement with previous reports [Powers and Binder, 2000; Prut and Perlmutter, 2003; Wohrer *et al.*, 2013]. The instantaneous firing rate in the control condition (0 nA) was lognormal as expected for the fluctuation–driven regime (top, **Figure 7E**). When adding input current the distribution was shifted to the right and enriched with a negative skewness as expected for mean-driven spiking (bottom, **Figure 7E**). This relation between input and shape of rate distribution was further confirmed by a negative correlation between multiple current injections and skewness both on linear scale (gray dots) and log–scale (red dots, **Figure 7F**). Hence, skewness and irregularity are indicators of the spiking regime.

Blocking inhibition causes change in regime

An alternative to injecting electrode current is to manipulate the balance of excitation and inhibition (E/I) by pharmacological means. This is important for understanding the cause of irregularity and the fluctuation–driven regime. Hence, we manipulated the synaptic input in a reduced preparation with micro–superfusion of strychnine, a glycinergic blocker, over the transverse cut surface of the spinal cord (described in [Berg *et al.*, 2007; Vestergaard and Berg, 2015]). This affected only neurons at the surface ($<300\mu$m) without affecting the rest of the network, which was verified by careful monitoring of flow and the network activity via the nerve recordings. Comparing the spiking during control condition (**Figure 8A**) with that during blockade of inhibition (**Figure 8B**), we noticed a strong increase in spiking. This is consistent with a depolarization due to disinhibition, thus 'unbalancing' the excitatory and inhibitory input. Reducing inhibition tipped the balance of E/I toward larger inward synaptic current, which resulted in a more depolarized V_m (blue line) well above threshold (arrows, **Figure 8A–B**). It also resulted in higher firing rates and lower irregularity on the

peak (cf. green lines). Generally, the irregularity (CV_2) was higher in the control case than in the unbalanced case (**Figure 8C**) similar to the results observed with current injection (**Figure 7A–D**). The irregularity was also negatively correlated with depolarization of the mean V_m when unbalancing the E/I although it was uncorrelated in the control condition, where the spiking occurred in the fluctuation–driven regime (**Figure 8 supplement 1**). The instantaneous firing rate was skewed and lognormal in the control case (top, **Figure 8D**), similar to the above sample cell (top, **Figure 7E**). This distribution became negatively skewed when adding inward current (bottom, **Figure 7E**). Similar effect was seen when 'unbalancing' the synaptic input, which also result in larger inward current. The firing rate increased (cf. broken lines, **Figure 8D**) and the distribution became negatively skewed (cf. -0.2 and -1.5) as expected in the mean–driven regime (bottom). To quantify the increase in time spent in the mean–driven regime, we performed an analysis similar to the analysis in the above section (**Figure 6D**). The cumulative time spent below threshold was larger in the control condition (78%) compared with the unbalanced case (56%, **Figure 8E**). These observations are largely consistent with the consensus view that irregular fluctuation–driven spiking is due to a balance between excitation and inhibition (**Table 1**).

CV_2 as an indicator of spiking regime

In the above intracellular analyses we reported the spiking irregularity in terms of CV_2 along with the mean V_m, current injection and pharmacological manipulation of the balance of excitation and inhibition. The CV_2 measure is convenient to use as an indicator of the mean– versus the fluctuation–driven regimes observed in the extracellular spiking data, since it only requires spike times. Therefore it is important to validate CV_2 as an indicator of spiking regime. In the above sample cell analyses we note first, that when V_m spent a larger fraction of time above threshold, i.e. in mean–driven regime, the CV_2 was lower (**Figure 6**). Second, when depolarizing a neuron artificially either with constant positive current (**Figure 7D**), or by blocking inhibition (**Figure 8C**), such that more spikes were in mean–driven regime, the CV_2 was decreased.

To further substantiate CV_2 as an indicator of spiking regimes we looked again at the return map ratio, which is an independent metric of fluctuations during inter-spike intervals. If CV_2 is an indicator of the spiking regime, it should be anti-correlated with the return map ratio. This was confirmed by plotting the mean CV_2 for all cells ($n = 68$) against the mean return map ratio, which indeed demonstrated a significant anti–correlation ($R = -0.34$, $P = 0.005$) (**Figure 3 supplement 1E**).

A second independent indicator of fluctuation regime is the cumulative time below threshold of V_m (**Figure 6D**), which should be correlated with the mean CV_2. We tested this using the most hyperpolarized value of theshold, since it was the most conservative, but there was no significant correlation between the cumulative time below threshold and the mean CV_2. Perhaps the lack of correlation is due to a bias from the reset voltage and after-hyperpolarization, which is different from cell to cell and therefore randomly may introduce a large fraction of time spent below threshold. Also, intense synaptic activity is known to quench the after–hyperpolarization [Berg *et al.*, 2008] and therefore this bias may be particularly strong when the synaptic input is not balanced as in the mean–driven regime.

A third indicator of spiking regime is the skewness of the instantaneous firing rate distribution (**Figure 7E** and **8D**). We estimated the skewness of the individual firing rate distributions for all neurons ($n = 68$) and plotted it against the mean CV_2 (data not shown). There was a significant positive correlation between the two, regardless of whether the firing rate distribution was plotted on log or linear scale ($R_{log} = 0.43$, $p = 0.0003$, and $R_{lin} = 0.41$, $p = 0.0006$), which suggest CV_2 as a valid measure for spiking regimes.

A last indicator is the local mean membrane potential depolarization, which should be anti-correlated with the instantaneous CV_2, if the V_m is above threshold (**Figure 8, supplement 1D**). Here, there was a lack of correlation between CV_2 and V_m before blocking inhibition, in the fluctuation–driven regime. However, after removal of inhibition, V_m was in supra–threshold domain, which introduced an anti-correlation between CV_2 and V_m. Hence, if the neuron is in the mean-driven regime the CV_2 is an indicator for the depolarization above threshold. To further verify this we performed a similar test of the relationship between instantaneous CV_2 and local depolarization for all neurons (without pharmacology). We found that all the cells with significant relationships ($p < 0.05$, $n = 16/68$) had anti-correlation between V_m and CV_2 (data not shown). In conclusion, the CV_2 measure is correlated with other measures and indicators of spiking regimes (except the cumulative time below threshold) and therefore CV_2 is a useful indicator in itself.

Noisy threshold has no effect

The irregularity in spiking could be caused by a noisy threshold rather than fluctuations in synaptic potentials. Nevertheless, a noisy threshold can only explain a small part (if any) of the spiking irregularity. First of all, if the irregularity, that we observed in spike times, was due to a noisy threshold mechanism, we should see the same irregularity regardless of the depolarization, i.e. regardless of whether the neuron was in the sub–threshold or supra–threshold domain. Yet, the spiking irregularity was strongly dependent on depolarization (**Figures 6, 7** and **8**). There was an adaptation in threshold (**Figures 6, supplement 1**). This was not random, but rather due to a gradual inactivation of Na^+–channels throughout the burst. The threshold of a given spike strongly depended on the threshold of the previous spike (panel F) as well as the mean firing rate (panel G). The same mechanism is behind spike–frequency adaptation, which is a well–described phenomenon [Grigonis *et al.*, 2016]. The adaptation in threshold is likely to make the IO-function more sublinear in the mean–driven regime, which will generally curb network activity.

In order to verify the extent of the threshold variance beyond the contribution from inactivation of Na^+–channels, we looked at the threshold of only the first spike of each cycle, such that the neuron had ample time for recovery. The variance of the first–spike threshold ($n = 51$) in a sample neuron was $\sigma^2_{thres} = 0.8$ mV^2 whereas the variance in synaptic potentials was more than 17–fold higher ($\sigma^2_{Vm} = 14.0$ mV^2). Therefore a randomness in the threshold had little of no effect on the irregularity of spiking compared with the randomness in synaptic input. In some recordings the threshold may appear as uncorrelated with the membrane potential prior to the spike onset. However, rather than a noisy threshold this is likely attributed to cellular morphology. If the cell is not electrically compact, the axon initial segment, where the spike is initiated, will have a different potential than what is recorded with the electrode. If this was the case, these observations would still be compatible with the two–regime hypothesis, since spikes would still be driven either by fluctuations or a large mean current, despite the disguise of a long electrotonic distance to the recording site.

Rich diversity in population firing rates

So far the analysis has been performed on serially acquired intracellular recordings across trials and animals. This demonstrates that some neurons spiked primarily in the fluctuation–driven regime while others spiked in the mean–driven regime. Nevertheless, it is still unclear what the parallel population activity was during a behavior and across behaviors. How many neurons were in one versus the other regime and for how long? First, we assessed the neuronal participation in the motor patterns by their degree of spiking during motor behavior. Neurons were active during both ipsi– and contralateral scratching behaviors (**Figure 9A–D**). Most units had a rhythmic relationship with the nerve signals and a higher firing rate for the ipsilateral scratching compared with contralateral scratching behavior (cf. **Figure 9C** and **D**; **Movie supplement 1** and **2**), which indicates participation of neurons in a hemicord to a smaller degree in the contralateral movement than the ipsilateral movement.

The distribution of firing rates across the neuronal population over several trials was strongly skewed, which indicate that most neurons spike relatively infrequently with a 'fat-tail' of higher spiking (**Figure 9E**). The distribution covered two orders of magnitudes from 0.1–10Hz and was akin to a lognormal distribution (inset and green lines, **Figure 9E**). Similar lognormal–like distributions have been observed in other parts of the nervous system [Buzsáki and Mizuseki, 2014]. The implication of the skewed distribution is that most neurons spiked at low rates, but there was relatively many neurons spiking at higher rates indicating an overall rich diversity of firing rates.

Skewness preserved across behaviors

Although multi–functional spinal units have been reported previously [Berkowitz *et al.*, 2010] it is unclear how their participation is distributed and whether the asymmetry in distribution is linked to different behaviors. To address this issue we analyzed the population spiking for multiple motor behaviors. The induction of a distinct scratch behavior is location–specific [Stein, 2005]. Multiple behaviors can be evoked depending on exact location and which side of the body is touched. This allowed us to induce two distinct behaviors: ipsi– and contralateral hindlimb scratching, while recording from the same neuronal ensemble (**Movie supplement 1** and **2**). These behaviors were reproducible over multiple trials (>9 trials). Both behaviors had similar phase relationships between the muscle synergists, although ipsilateral scratching had stronger activity (cf.

Figures 9A and **B**). The firing rate distribution was positively skewed in both behaviors with the similar qualitative shape (**Figure 9E-F**). This skewness was also found across animals (green bars, **Figure 9G**, n=5) and close to zero on log–scale, i.e. lognormal (black lower bars). To further quantify the uneven neuronal participation we used Lorenz statistics and the *Gini-coefficient* [Ikegaya *et al.*, 2013; O'Connor *et al.*, 2010]. The Lorenz curve characterizes the share of cumulative participation of individual neurons of the population (**Figure 9H**). The diagonal corresponds to the case where all neurons have the same firing rate. The deviation from equality is quantified by the Gini–coefficient, which is the fraction of area a to the total area $a + b$ (**Figure 9H**). The higher the coefficient, the more unequal the participation across neurons is. Both scratch behaviors had a Gini–coefficient of $\sim$0.5 (**Figure 9I**), though the ipsilateral behavior had a slightly higher Gini–coefficient (greater inequality). Although the mean firing rate could change between behaviors and between animals (**Figure 9J**), the skewness was qualitatively similar (**Figure 9K**). This suggests that the skewed lognormal–like firing rate distribution, and hence a presence of the fluctuation–driven regime, was preserved across behaviors and animals.

Skewness in firing rate distribution is activity–dependent

Neurons do not occupy either the fluctuation– or the mean– driven regime all the time. Individual neurons can move back and forth between regimes depending on the synaptic current they receive. Neurons that spike predominantly in the mean–regime will have their means firing rate closer together and more normally distributed compared with those spiking in the fluctuation–regime. Hence, we expected the skewness of the distribution of mean firing rates across the population to become more negative (on log–scale) as the general network activity increases. To address this, we analyzed the spiking across neurons in parallel. First, we estimated the time–dependent firing rate of each neuron in the population using optimal Gaussian kernel [Shimazaki and Shinomoto, 2010] and measured skewness of the population distribution. The time–dependent population distribution was achieved by binning the rates in 10 ms windows (**Movie supplement 1** and **2**). The mean population rate and its SD are indicated as black $\pm$ gray lines (**Figure 10A**). As the mean firing rate increased, the skewness of the distribution (log–scale) became negative, which is a sign of more neurons were occupying the mean–driven regime (cf. inset histograms, **Figure 10A**). This was further confirmed by a negative correlation between the mean firing rate (black line in A) and the log–skewness for all time points (**Figure 10B**). Hence, as the general activity increased, the population distribution became less lognormal and more Gaussian, which suggests more neurons occupied the mean–driven regime during a higher general activity.

Occupancy within regimes across population and time

To further gauge the division of neurons in the two regimes we compared the irregularity of the spiking using CV_2. This metric was verified above as a reliable indicator of spiking regimes. The distribution of the mean CV_2 across the population of neurons was clustered around 1 if all ISIs were included (gray histogram, **Figure 10C**). However, measuring the irregularity in the motor cycles alone i.e. excluding the inter–burst intervals (here, $ISI < 0.5$s) the mean irregularity across neurons was lower and clustered around 0.6 (red histogram). Both distributions had substantial spread around the mean, which suggests a rich diversity spiking patterns.

To get a compound measure of the behavior of the entire population across time, we considered the amount of time each neuron spent in the fluctuation–driven regime. We demarcated the fluctuation–regime as having irregularity in spiking above a critical value, i.e. $CV_2 > i_{crit}$. Choosing i_{crit} is not entirely objective. Complete Poisson–type irregularity has $CV_2 = 1$, but the spiking is still irregular for lower values [Feng and Brown, 1999]. Based on our data, even when the $CV_2 \approx 0.5$, the V_m spent as much as 96% of the time below threshold (**Figure 6C–D**) indicating fluctuation–driven spiking. Further, neurons that had $CV_2 \approx 0.5$, also had lognormal firing rate distributions (**Figure 7**), which also indicates the fluctuation–driven regime. For these reasons, we suggest choosing $i_{crit} = 0.5$ for distinguishing regular vs. irregular spiking. A similar value was previously chosen to distinguish between regular vs. irregular 'choppers' in the cochlear nucleus [Young *et al.*, 1988]. Thus, the population of spinal neurons had a large diversity in time spent in the fluctuation–driven regime. Some neurons spent as little as 20% in the fluctuation–driven regime while other spent as much as 80%. To get a quantitative handle on the occupation of neurons in the fluctuation–driven regime across the population, we considered the distribution of time spent with $CV_2 > i_{crit}$. This was formally

quantified using the reverse cumulative distribution of neurons that spend a given fraction of time in the fluctuation–driven regime (**Figure 10D**). The reverse cumulative distribution is plotted for 3 values of i_{crit} (0.4, 0.5 and 0.6) to indicate the sensitivity to parameter choice. Obviously, choosing a lower i_{crit} results in a larger fraction of in the fluctuation–driven regime, i.e. the curve is shifted to the right. Choosing i_{crit} larger has the opposite effect. This inverted S–shaped curve gives the fraction of neurons (y–axis), which spend at least a given time in the fluctuation–driven regime normalized to 100% (x–axis). Hence, half of the population spent at least 58% of time in the fluctuation regime during ipsilateral scratching (intercept of curve with the broken line, **Figure 10D**). We refer to this metric as the *time in the fluctuation–regime for half the neurons* (TIF_{50}). Similar TIF_{50}–values were obtained for all five animals (inset histogram). Qualitatively similar results were achieved for a different motor behavior, namely contralateral scratching (**Figure 10E**). The TIF_{50} metric is a time–weighted analysis of irregularity of spike trains. In addition to measuring the time in regimes, we measured how many spikes were in one regime vs. the other. Hence, we calculated the reverse cumulative distribution of neurons that had a given fraction of spikes in the fluctuation–driven regime (**Figure 10 supplement 1**). Similar to TIF_{50}, we defined a spike–weighted metric as the *spikes in fluctuation regime for half the neurons* (SIF_{50}). Both the SIF_{50}– and TIF_{50}–values were relatively conserved across animals as well as behaviors (**Figure 10D–E**, **supplement 1**). The large values of TIF_{50} and SIF_{50} indicate that the fluctuation–driven regime had a strong presence during motor behaviors, and the high similarity suggests that it may represent a conserved fundamental property of network activity.

Cell types and spiking activity

In the data analyses presented so far we have not addressed the neuronal identity of the recorded units. Nevertheless, there is a spatial division subtypes of spinal neurons, which we could take advantage of. During development, a distinct laminar organization of different cellular subtypes is formed in the dorsoventral axis [Arber, 2012; Jessell, 2000]. In particular, motoneurons are primarily found in the most ventral part of the horn whereas interneurons are found in more medial to dorsal territory. Since this is the same axis that our electrode arrays were located along, it was possible to infer a likelihood of cellular identity based on location. The electrode shanks have multiple distributed electrodes (**Figure 11A**), which made it possible to approximate the soma location using *trilateration*. Trilateration is the geometrical process of determining the location of a source in space using multiple recording sites combined with the fact that signals decay in the extracellular space [Manolakis, 1996]. Thus, the node locations were approximated based on the amplitude of spike waveforms, which clearly decayed with distance (**Figure 11B**). Node locations were combined for all shanks, probes and animals to form a scatter (**Figure 11C**). Combining these locations with depth of individual shanks with respect to the surface of the spinal cord, we were able to investigate the spike patterns with respect to the absolute neuronal location. The irregularity in spiking was quantified (mean CV_2) with respect to dorsoventral depth (**Figure 11D**). The distributions of mean firing rates (not shown) and the mean CV_2 (**Figure 11E**) had no obvious dependence on depth. In particular, the spread in means was much smaller than the SD of the distributions themselves. The most parsimonious interpretation of these data is that the fluctuation–driven spiking regime was both present and equally prominent in all the neurons, regardless of whether the cell body was in the ventral horn or in the medial horn, i.e. equally present in motoneurons and interneurons.

DISCUSSION

In neuronal networks, spikes are generated in either in the *mean*– or the *fluctuation–driven regime* [Brunel, 2000; Gerstner *et al.*, 2014; Kuhn *et al.*, 2004; Tiesinga *et al.*, 2000]. In this report we present evidence for the existence of both regimes during motor pattern generation in the spinal cord. We consistently found normally distributed synaptic input combined with the supralinear shape of the IO–function in the subthreshold region, and suggest this as a compelling mechanism behind the lognormal population firing rate distribution [Roxin *et al.*, 2011]. Using spiking irregularity across the neuronal population as a hallmark of the fluctuation regime, we found that half of the neurons spend at least 50% of the time in this regime. Thus, the fluctuation–regime was not a rarity, but rather had a prominent presence both across behaviors and across animals (**Figure 10**). To our knowledge this is the first report, which quantifies occupation within spiking regimes of a neuronal population, not just in the spinal cord, but also in the nervous system in general.

Stability and the two regimes

The fact that the relative time during which a subset of neurons occupied one of the two regimes was conserved across both behaviors and animals could indicate a key principle of neuronal processing. A fundamental challenge for neuronal networks is to perform functions while keeping the population activity from falling into either of the two extreme states: 1) the quiescent state where the neuronal spiking activity cannot remain self–sustained and 2) the unstable state of run–away recurrent spiking activity [Kumar *et al.*, 2008; Vogels *et al.*, 2005]. It is well known that recurrent inhibition is important for maintaining stability, but other mechanisms may participate as well, e.g. synaptic depression or active adjustment of the shape of the neuronal response function by adaptation of spiking threshold. A nonlinear response function, as we observed in the fluctuation–regime (**Figure 4B**), will amplify input via supralinear summation [Rubin *et al.*, 2015]. The upward curvature will enhance synaptic fluctuations, which then accelerates the recurrent excitatory activity causing a potentially unstable state. In contrast, the response function in the mean–driven regime, is linear or even sublinear, which is likely to curb strong input. We therefore propose that the close proximity of the TIF_{50}–value to 50% is an indication of a self–organizing trade–off between sensitivity and stability in order to preserve at once both network homeostasis and dynamical functionality. This conjecture remains to be further substantiated in future studies. Furthermore, the TIF_{50}– and SIF_{50}–values remain to be determined for other part of the nervous system and in other species.

Rhythm generation and regimes

The distinction between fluctuation– and mean–driven spiking is interesting because the two types of spiking may have radically different causes, and this may hold an important clue to understanding the enigmatic motor rhythm generation. The fluctuation–driven spiking is believed to be caused by concurrent and random arrival of excitatory and inhibitory potentials resulting in a fluctuating subthreshold V_m (**Table 1**). In the mean–driven regime, on the other hand, the net membrane current is so large that the mean $V_m \pm \sigma$ is above threshold, and the ISIs are therefore determined by the recharging of the membrane capacitance following the refractory period of the previous spike [Powers and Binder, 2000]. This results in a deterministic trajectory of V_m and regular ISIs. More importantly, for the mean–driven spiking the membrane current can be caused by intrinsically electrical properties [Llinas, 2014] as well as synaptic input, whereas the fluctuation–driven spiking is exclusively caused by synaptic input. An intrinsic property, which is commonly believed to be involved in rhythm–generation, is the pacemaker property that can autonomously generate neuronal bursting in the absence of synaptic input [Brocard *et al.*, 2010]. The prominent presence of the fluctuation–regime therefore implies that the majority of neuronal spikes were not driven primarily by intrinsic properties such as pacemaker potentials, but rather by synaptic communication. This can be interpreted in two ways: 1) if there is a pacemaker–driven rhythmogenic core of oscillatory neurons responsible for the motor activity [Huckstepp *et al.*, 2016], the core only represents a small fraction of the network, or 2) since the fluctuation–regime is prominent and pacemaker neurons are difficult to find, the motor–rhythm may be generated by other means such as emergent collective processes in the network [Yuste, 2015]. Generation of movements without the need of pacemaker neurons have been predicted theoretically in central pattern generators [Kleinfeld and Sompolinsky, 1988] as well as more complex sequence generation [Hennequin *et al.*, 2014]. Even in the respiratory system, which has the most stereotypic motor rhythm, pacemaker cells appear not to be essential for generation of the rhythmic breathing, although this topic is still debated [Feldman *et al.*, 2013]. It remains to be understood how a distributed emergent processes can generate motor rhythms on a network level if, in fact, the pacemaker bursting is not an essential component.

Cell identity and circuit function

In spinal research, neuronal identification has improved over the last decades with the development of genetic knockouts and molecular markers [Bikoff *et al.*, 2016; Britz *et al.*, 2015; Goulding, 2009; Kiehn, 2006]. Pinning down cellular identity improves the search for a potential specialization in the circuit. However, the sole focus on cellular identity to address questions in spinal research carries a weakness as well as a strength. It contains the risk of missing the collective dynamics and the delicate interaction among neuronal cell types. Neural circuits operate to perform functions by collective interaction between all neurons, where it is difficult, if not impossible, to link a particular function to the individual neuron. Functional activity may very well arise

on circuit level as opposed to cellular level. This caveat is known as the *neuron doctrine* versus emergent network phenomena [Grillner, 2006; Yuste, 2015], and the neuron doctrine has almost exclusively been adopted in previous investigations of spinal motor circuits. To the best of our knowledge this report is the first investigation of spinal motor circuits from an ensemble viewpoint.

Nevertheless, since motoneurons are fundamentally different from the rest of spinal neurons it would be helpful to distinguish them from interneurons. In our experiments we sampled from neurons, which were likely to be primarily interneurons since they are more numerous than motoneurons. The fraction of motoneurons to interneurons is 1:8 [Walloe *et al.*, 2011], but we were also likely to sample motorneurons, since they have large somata. To explore this further, we investigated the population activity and its relation to cellular identity by taking advantage of their spatial segregation in the dorsoventral axis [Arber, 2012; Jessell, 2000]. We were able to associate an absolute location of the cellular somata (using trilateration), and thus test for differences in spiking activity (**Figure 11**). The distribution of firing rates as well as the spiking irregularity did not have any dependence on location. This suggests that the fluctuation–driven spiking regime was both present and equally prominent in all the neurons, regardless of whether the cell bodies were in the ventral or medial horn, i.e. regardless of whether they were motoneurons or premotor interneurons.

Comparison with other parts of the CNS

Common features of network activity for different parts of the central nervous system may provide hints towards fundamental principles of neuronal operations. In the present study we identified the following features of population motor activity: 1) synaptic input to individual spinal neurons was normally distributed (**Figure 3**), 2) the means of these normal distributions were also normally distributed across the population. In particular, the distance to threshold in terms of fluctuations, i.e. $(V_m - V_{thres})/\sigma$ had a normal distribution and a distance from mean to threshold of 3σ on average (**Figure 3 supplement 2F**). 3) The neuronal response function was supralinear when the mean input was in the subthreshold region (**Figure 4B**). 4) There was a rich diversity of regular to irregular spiking patterns. 5) The population firing rate was skewed and lognormal–like.

Many of these features have been identified before in other parts of CNS. The V_m of individual neurons is often normally distributed in cortical neurons when considering either the up– or down–state [Destexhe *et al.*, 2003; Stern *et al.*, 1997] and the spiking is irregular with a CV clustered around 1 [Softky and Koch, 1993; Stevens and Zador, 1998]. Similar irregularity is observed in non-vertebrates [Bruno *et al.*, 2015]. The distribution of mean CV_2 values in our experiments was clustered around 0.6 when ignoring the inter–burst intervals (**Figure 10C**). This is more regular than what is observed for typical cortical neurons (although see [Feng and Brown, 1999]), but similar to cervical interneurons in monkeys performing isometric wrist flexion–extensions [Prut and Perlmutter, 2003].

Lognormal population firing

We observed a skewed and lognormal–like population distribution across behaviors (**Figure 9**, **Movie supplement 1** and **2**). Similar lognormal distributions have been reported in other parts of CNS [Buzsáki and Mizuseki, 2014; Hromádka *et al.*, 2008; O'Connor *et al.*, 2010; Wohrer *et al.*, 2013] and it remains an open question how the skewness arises out of neuronal ensembles. *Roxin et al* proposed the mechanism where the skewness arises from a nonlinear transformation of Gaussian input [Roxin *et al.*, 2011]. Our data supports this hypothesis. First, we observed a a normally distributed V_m for individual cells, which is a proxy for the requirement of normally distributed input currents (**Figure 3**). Second, a supralinear IO–function covering most of this input (**Figure 4**). Third, a firing rate distribution of individual cells which was typically highly skewed and lognormal–like although some did not have lognormal firing (**Figure 5**). Nevertheless, there is a distinction between the lognormal firing of individual neurons and the lognormal distribution of mean rates across the population. Whereas the lognormal population firing rate remains to be fully understood, the skewed firing rate distribution of individual neurons is fairly well understood. Here, the skewness is due to the fluctuating input and irregularity of spiking [Ostojic, 2011]. Nevertheless, we argue the mechanism for the lognormal population firing is the same as that for the individual neuron. If the subthreshold IO-function is approximately similar across the population, which our data implies (**Figure 4**), we can explain the lognormal population firing by a supralinear transformation, if the mean V_m across the population is also Gaussian. We

did in fact find the distribution of mean V_m to be Gaussian (**Figure 3 supplement 2F**).

Fluctuation–driven regime as a subprimary range in motoneurons?

Classical studies of spinal motoneurons indicate two regimes of spiking: a primary and a secondary range [Kernell, 2006; Meehan *et al.*, 2010], which corresponds to different parts of the mean–driven spiking regime. This characterization was associated with the intrinsic properties without synaptic input being present. Nevertheless, a different type of fluctuation–driven spiking was discovered in experiments where synaptic input were present, in what was referred to the *subprimary range* in mice [Manuel and Heckman, 2011] and humans [Kudina, 1999; Matthews, 1996]. This subprimary range conforms to the fluctuation–regime though under a different terminology. As the name indicates, the primary range has been considered to represent the dominant mode of spiking whereas the subprimary range is a peculiarity. Nevertheless, a recent study recorded for the first time the motoneuron discharge and muscle force and found that the subprimary range accounts for 90% of the contraction force [Manuel and Heckman, 2011]. This indicates that the fluctuation–regime may have a more noteworthy role in covering the dynamical range in motor control than previously assumed, which is in agreement with the observations of the present study.

Materials and Methods

Experimental procedures

We used the integrated turtle preparation with the spinal motor network intact ($n = 5$ for the multi–electrode recordings and $n = 60$ for the serially aqquired intracellular recordings), in order to address how the neuronal firing rates are distributed across the population of interneurons and motoneurons in the spinal cord [Petersen *et al.*, 2014]. These sample sizes where assumed to be large enough in the experimental design and because of a consistency in results, although a specific power analysis was not conducted. To avoid the confounding factors of supraspinal input, we spinalized the turtle. The transection was performed at the spinal cord at segments (D3-4) caudal to the cervical segments, where the local circuitry has only little or no involvement in generation of motor patterns [Hao *et al.*, 2014; Mortin and Stein, 1989; Mui *et al.*, 2012]. The adult turtle preparation is capable of producing elaborate motor patterns such as scratching. We used the semi-intact spinal cord of adult turtles [Keifer and Stein, 1983; Petersen *et al.*, 2014] and recorded from the segments D8-D10. These segments contain the essential CPG circuits [Mortin and Stein, 1989]. Most of the spinal cord including the sensory periphery is left intact. The blood is replaced and the spinal column is provided with oxygenated Ringers solution so that the neurons and the network have optimal conditions. In this experimental situation the motor behavior is as close to *in vivo* situation as possible, and is indistinguishable from the intact condition [Keifer and Stein, 1983]. The turtle preparation allow for mechanical stability and the turtle's resistance to anoxia allow for remarkable durability of both the recording conditions and the motor pattern reproducibility [Vestergaard and Berg, 2015].

Integrated Preparation Adult red-eared turtles (*Trachemys scripta elegans*) of either sex were placed on crushed ice for 2 hours to ensure hypothermic anesthesia. The turtles were killed by decapitation and the blood was substituted by the perfusion with a Ringer's solution containing (mM): 100 NaCl; 5 KCl; 30 $NaHCO_3$; $2MgCl_2$; $3CaCl_2$; and 10 glucose, saturated with 95% O_2 and 5% CO_2 to obtain pH 7.6, to remove the blood from the nervous system. We isolated the carapace containing the spinal cord segments D4-Ca2 by transverse cuts [Keifer and Stein, 1983; Petersen *et al.*, 2014] and perfused the cord with Ringer's solution through the *vertebral foramen*, using a steel tube and gasket pressing against the D4 vertebra. We opened the spinal column on the ventral side along D8-D10 and gently removed the dura mater with a fine scalpel and forceps. For each insertion site for the silicon probed, we opened the pia mater with longitudinal cuts along the spinal cord with the tip of a bend syringe needle tip (BD Microlance 3: $27G3/4$",$0.4x19mm$). We performed the cuts parallel to the ventral horn between the ventral roots. The surgical procedures comply with Danish legislation and were approved by the controlling body under the Ministry of Justice.

Network Activation We used a fire polished tip of a bent glass rod for mechanical stimulation, that was mounted linear actuator. The actuator was controlled with a function generator: frequency, amplitude and

duration of the stimulus.

Extracellular Recordings Extracellular recordings were performed in parallel at $40kHz$ using a 256 channel multiplexed Amplipex amplifier (KJE-1001, Amplipex). Up to four 64-channel silicon probes were inserted in the incisions perpendicular to the spinal cord from the ventral side. We used the 64-channel Berg silicon probes (Berg64 from NeuroNexus Inc., Ann Arbor, MI, USA) with 8 shanks, and 8 recording sites on each shank arranged in a staggered configuration with $30\mu m$ vertical distance. The shanks are distanced $200\mu m$ apart. Recordings were performed at depths in the range of 400-1000μm.

Intracellular Recordings The intracellular recordings were performed in current-clamp mode with an Axon Multiclamp 700B amplifier (Molecular devices). Glass pipettes were pulled with a P-1000 puller (Sutter instruments) and filled with a mixture of 0.9 M potassium acetate and 0.1 M KCl. Data were sampled at about 20 kHz with a 12-bit analog-to-digital converter (Axon Digidata 1440a, Molecular devices). We inserted the glass electrodes from the ventral side of D8-D10 perpendicularly to the spinal cord. Neurons were located at depths ranging from about 300-800μm. Typically we had stable intracellular recordings for multiple trials.

Nerve Recordings Electroneurogram (ENG) recordings were performed with suction electrodes. The scratch behavior was measured by the activity of the nerves: Hip Flexor, Knee Extensor, dD8 and HR-KF. The nerve activities were recorded with a differential amplifier Iso-DAM8 (World Precision Instruments) with bandwidth of $100Hz - 1kHz$.

Histology For histological verification, we combined several staining techniques: The silicon probes were painted with DiI ($1-2\%$ diluted in ethanol) before insertion into the spinal cord [Blanche *et al.*, 2005; Vandecasteele *et al.*, 2011]. Following successful experiments, we performed Nissl– and ChAT–staining of the tissue, to determine the location of respectively neurons and motoneurons.

The histological processing is detailed in Petersen *et al.* [2014]. We carefully removed the tissue, perfused it and put it in phosphate buffered saline (PBS) with 4% paraformaldehyde for 24–48 hrs and further stored it in PBS. The tissue was mounted in an agar solution and sliced into $100\mu m$ slices using a microtome (Leica, VT1000 S). The slices were washed with PBS and incubated overnight at 5^oC with primary choline acetyltransferase antibodies goat anti-ChAT antibodies (1:500, Milipore, USA) in blocking buffer, which is PBS with 5% donkey serum and 0.3% Triton X-100. The slices were washed three times with PBS and incubated for 1 hr at room temperature with the secondary antibody Alexa488 conjugated to donkey anti-goat antibodies (1:1000 Jackson) in blocking buffer. After three washes with PBS, the slice was mounted on cover slit with a drop of ProLong Gold antifade reagent (Invitrogen Molecular Probes, USA) and cured overnight at room temperature before microscopy. The slice was viewed using a confocal microscope, Zeiss LSM 700 with diode lasers, on a Zeiss Axiolmager M2 using 10x/0.30 EC Plan-Neofluar, 40x/0.6 Corr LD Plan-Neofluar, and 63x/1.40 oil DIC Plan-Apochromat objectives (Zeiss).

Data Analysis

The data analysis was primarily done in the programming languages Matlab and Python. The correlation coefficient was calculated as the Pearson product-moment correlation coefficient.

Skewness of distribution We use *skewness* [Press *et al.*, 1992] or the third moment as a measure of asymmetry in the distribution around the mean, sometimes referred to as Pearson's moment coefficient of skewness. It can be estimated using the method of moment estimator as

$$Skewness = \frac{1}{N}\sum_{j=1}^{N}\left[\frac{x_j - \bar{x}}{\sigma}\right]^3 \quad (1)$$

where $x_1, ..., x_N$ are all the observations (V_m or firing rate) and σ and $\bar{x}$ are the sample standard deviation and sample mean of the distribution. The skewness is a unitless number and a value of zero indicates perfect symmetry. A positive skew has a tale pointing in the positive direction of the axis and a negative value points in the opposite direction.

Spike Sorting Spike sorting was performed in the Klustakwik-suite: SpikeDetekt, KlusterKwik v.3.0 and KlustaViewa [Kadir *et al.*, 2014]. Raw extracellular signals were bandpass filtered from $400 - 9000Hz$, and spikes were detected by a median based amplitude threshold with SpikeDetekt [Kadir *et al.*, 2014; Quiroga *et al.*, 2004; Takekawa *et al.*, 2012]. An automatic clustering of the spikes was performed in KlustaKwik, followed by manual cluster-cutting and cluster verification in KlustaViewa. The cluster quality was evaluated by several measures: The shape of the autocorrelation function, the amount of contamination in the refractory period, the Isolation distance [Harris *et al.*, 2001] and the L_{ratio} [Schmitzer-Torbert and Redish, 2004] (**Figure 2 supplement 2**). Only well isolated units was used in the further data analysis.

Time-dependent Firing Rates The time-dependent firing rate were estimated by a gaussian kernel. Spike times $x(t)$ were convoluted with a kernel $k(t)$ to estimate the instantaneous firing rate

$$rate(t) = \int_{-\infty}^{\infty} x(t - t')k(t')dt' \tag{2}$$

where $k(t)$ is defined as

$$k(t) = \frac{1}{\sqrt{2\pi}\omega} e^{-\frac{t^2}{2\omega^2}} \tag{3}$$

with the bandwidth ω optimized for each spiketrain with the sskernel method [Shimazaki and Shinomoto, 2010]. The estimated width was in the range of $100 - 500\mu s$.

Gini Coefficient The *Gini* coefficient is a measure of statistical dispersion and it is defined as a ratio of the areas on the Lorenz curve diagram

$$Gini = \frac{a}{a+b} = 1 - 2b \tag{4}$$

where $a + b$ is the area below the line of no dispersion (the diagonal, i.e. $a + b = 1/2$), and b is the Lorenz curve, i.e. the cumulative distribution of firing rates (**Figure 9H**).

Irregularity of the Spiking Activity The irregularity of the spiking of individual neurons can be described by several measures. The most common measures are the coefficient of variation ($CV = \sigma/\mu$) and the Fano factor ($F = \sigma^2/\mu$), but both measures easily overestimate the irregularity when the firing rate is non-stationary [Holt *et al.*, 1996; Ponce-Alvarez *et al.*, 2010; Softky and Koch, 1993]. More advanced methods of estimating the time dependent variations in the irregularity have been developed [Miura *et al.*, 2006; Shimokawa and Shinomoto, 2009; Shinomoto *et al.*, 2009], and here we use the widely used metric CV_2, which has been suggested to be the most robust measure of local spiking irregularity [Ponce-Alvarez *et al.*, 2010; Wohrer *et al.*, 2013]. The time dependent CV_2 is defined by pairs of adjacent inter-spike intervals ISI_i and ISI_{i+1}:

$$CV_2(i) = \frac{2|ISI_i - ISI_{i+1}|}{ISI_i + ISI_{i+1}} \tag{5}$$

where $CV_2 = 1$ for a Poisson process and $CV_2 = 0$ for a regular process. CV_2 can take values in the range from zero to two.

We noticed a small difference in the distribution of irregularity among the neurons recorded with intracellular versus extracellular electrodes (data not shown). The neurons were recorded with intracellular electrodes had more regular spiking than those recorded with extracellular electrodes. This may be caused by a systematic bias in the way the intracellularly recorded neurons were collected, as there is an experimental bias towards high firing rates. Spike sorting processing of the extracellular recordings, on the other hand, is likely to both miss spikes and contain false positives, which will cause overestimation of spiking irregularity.

TIF_{50} and SIF_{50}: time and spikes in fluctuation regime based on spiking irregularity To get a quantitative handle on the fraction of neurons found in the fluctuation–regime across the population, we consider the distribution of neurons, $f(t)$, which spends a given amount of normalized time t in the fluctuation regime, i.e. with $CV_2 > i_{crit}$. We consider three values of i_{crit}, 0.4, 0.5 and 0.6, as indicators for when the neurons are in the fluctuation–regime. Formally we quantify the time in fluctuation–regime for the population using the

reverse cumulative distribution of neurons (**Figure 10D–E** and **supplement 1**). The reverse cumulative fraction of neurons in the fluctuation regime $F(t)$ for a given fraction of normalized time t is

$$F(t) = 1 - \int_0^t f(t)dt,\ 0 < t \leq 1 \tag{6}$$

This fraction $F(t)$ is the fraction of neurons, which spend at least t amount of normalized time in the fluctuation regime. To compress the distribution into a single number we use the fraction of time in fluctuation regime of half of the population, TIF_{50}, which is the value of t for which $F(t) = 50\%$ (arrows and broken lines, **Figure 10D–E**).

Since the firing rate is rarely constant, one may want to know how many spikes are elicited in the mean–versus fluctuation regime. This is calculated in similar way, using the distribution of neurons having a normalized fraction of spikes in the fluctuation regime, i.e. spikes with $CV_2 > i_{crit}$, $f(s)$. The reverse cumulative of $f(s)$ again gives the fraction of neurons which have at least s spikes in fluctuation regime, normalized to 100%,

$$F(s) = 1 - \int_0^s f(s)dt,\ 0 < s \leq 1 \tag{7}$$

Again we compress the distribution into a single number and use the fraction of spikes, which occur in fluctuation regime of half of the population, SIF_{50}, which is the value of s for which $F(s) = 50\%$ (arrows and broken lines **Figure 10 supplement 1**).

Estimating threshold We use a definition of the action potential threshold, which is based on the phase plot of V_m versus the derivative dV_m/dt. This is the second method reported in Sekerli *et al.* [2004]. The threshold is found as the point in the trajectory in phase space, where there is a strong departure from rest prior to the cycle. Since dV_m/dt is proportional to the membrane current, this point represents a strong initiation of the inward current. Defining the slope of V_m in time, $f = \frac{dV_m}{dt}$, the threshold is defined as the largest peak in second derivative with respect to V_m in phase space, i.e. the maximum of $\frac{d^2f}{dV_m^2}$ (red dots, **Figure 6 supplement 1B–C**). This is the point with the largest acceleration from baseline prior to the peak of the action potential. The V_m trace was low–pass filtering at 5000 Hz to reduce the vulnerable to electrical noise of the estimates of derivatives.

Spike rate versus V_m (FV-curve) The method for estimating the response rate as a function of V_m has been described previously [Vestergaard and Berg, 2015]. First, we empirically determine the stochastic distribution of V_m prior to the spike (1.5-1.7 ms prior) of neurons in the fluctuation–driven regime (as assessed by the return map ratio method). Then we normalize this distribution with the total amount of time spent at each V_m-level at all time. This is the probability of getting a spike within a small time window for a given membrane potential. This is empirical probability of getting a spike in a short time–window, i.e. the spike rate, as a function of V_m [Jahn *et al.*, 2011]. It is analogous to poisson processes under the assumption that the spiking can be considered a renewal process. The shape of the spike response function is highly non-linear with upward curvature. This has been observed in previous experiments often referred to as expansive non-linearity [Hansel and van Vreeswijk, 2002; Miller and Troyer, 2002; Murphy and Miller, 2003; Priebe and Ferster, 2005, 2008]. An exponential

$$R(V_m) = ce^{\beta V_m} \tag{8}$$

was fitted to capture the curvature, where the curvature is represented in the exponent β, which have units of $1/mV$, and c is a constant of units $1/s$. Such expansive non-linearities have also been investigated in the visual cortex where they are often characterized as a power-law relationship, i.e.

$$R(V_m) = k[V_m - E_a]^\alpha \tag{9}$$

where k is a constant and α is the power > 1, i.e. supralinear, and often ranging from 2-5 [Hansel and van Vreeswijk, 2002; Miller and Troyer, 2002]. This exponent is also a measure of the expansive curvature of the non-linearity. E_a represent a subthreshold level of V_m, where the spiking probability is zero, such that the values in the sampled traces are always larger than E_a, i.e. $V_m > E_a$. The curvature dependence on synaptic fluctuations was assessed by the standard deviation of the distribution of V_m traces prior to the spike in the

diffusion regime, i.e. where there was no link to the V_m and the spike occurrence. This distribution was chosen 18 ms prior to the spike (**Figure 3B**). The analysis and fits were performed in Matlab with generic fitting functions.

Return Map Ratio: Intracellular metric for mean– vs. fluctuation–regime In order to distinguish neurons in fluctuation– versus mean–regime, we employ a new metric for quantifying the degree of fluctuations in V_m in between action potentials. We plot the values of V_m in a return map, which is a plot of $V_m(t)$ versus $V_m(t + \Delta t)$. If the inter–spike V_m has a direct trajectory from the reset potential to the next spike, V_m will smoothly increase and thus $V_m(t + \Delta t)$ will always be larger than $V_m(t)$. Therefore each point will be above the line of unity (**Figure 3 supplement 1A–B**). On the other hand, if V_m has fluctuations, it will have an indirect and convolved trajectory from the reset value to the threshold. This will manifest as containing values of $V_m(t + \Delta t)$ which are actually smaller than $V_m(t)$. Thus we use the ratio of points above versus below the unity line as a metric for how convolved and fluctuating the path of V_m is from reset to threshold. If the ratio is $\sim$0.5 then V_m is highly fluctuating, whereas if the ratio is approaching 1 the path is straight without any fluctuations. We choose a mean value of the histogram of all values to 0.7 to classify neurons as fluctuation– or mean–driven (**Figure 3 supplement 1C**). This metric of straight versus convolved trajectory had significant negative correlation with other measures of fluctuation– regime, e.g. spike rate skewness, spike irregularity (CV_2) and *least time below threhold* (LTBT, **Figure 3 supplement 1D–F**). The choice of Δt is not important as long as it is larger than the timescale of electronic fluctuations of the amplifiers and smaller than the timescale of synaptic fluctuations in V_m. We consistently used $\Delta t = 1.5$ ms for all neurons. The return map ratio is intended as a metric to analyze sub-threshold activity and therefore spikes were removed from the traces, including a 6 ms window before and after the peak. Also, the V_m containing the interburst (defined as having ISIs $> 300ms$) intervals was removed.

Determining cellular location using trilateration Trilateration is a geometrical process of determining the location of a source in 2D–space using multiple recording sites scattered in space. We adapted the method to take advantage of a distance–dependent decay of the electrical signal from the action potential in the extracellular space. In this way, the amplitudes of the waveforms, which were simultaneously recorded on multiple electrodes, revealed the location of the source in space relative to the position of the electrodes. We assumed that the electrical signal decayed as $1/r^2$, where r is the distance.

Data selection

In figure 6, the following trials were used: $n = [6, 4, 9, 5, 6]$ for ipsilateral pocket scratch and $n = [6, 3, 10, 5, 6]$ for contralateral pocket scratch. Data used in **Figure 7** has already been published in a different context [Berg *et al.*, 2007]. A small subset of the neurons used in **Figure 3D–E** ($n = 10$ out of 68) has been acquired in a reduced preparation [Petersen *et al.*, 2014] and published for an investigation of a different matter [Berg and Ditlevsen, 2013; Berg *et al.*, 2007]. The data from experiments of blockade of inhibition using superfusion of strychnine has also been published previously in the investigation of a different matter [Vestergaard and Berg, 2015]. Regarding excluding spikes from the analysis in **Figure 3C–E**: For the temporal distribution (panel C), only ISIs$> 6ms$ was included and for the spike triggered V_m-distribution only ISIs$> 20ms$ was included, all having ISIs$< 300ms$. Estimating the FV-curve (**Figure 4**) all spikes having ISIs$> 1.7ms$ was included.

Definition of fluctuation– and mean–driven spiking

Neuronal spiking has traditionally been considered to occur when the mean inward current of the cellular membrane is large enough to cross the rheobase such that the mean membrane potential (V_m) is above threshold (V_{thres}). In practice, the mean V_m will not exceed V_{thres} by very much due to the active spiking and after–hyperpolarization, but if this mechanism was turned off the mean membrane current (I_m) would drive V_m across threshold, formally written as $I_m > V_{thres}/R_m$ where R_m is the membrane resistance. Spikes elicited in this manner are in the *mean–driven* regime [Gerstner *et al.*, 2014; Renart *et al.*, 2007]. They have shorter inter–spike intervals (ISIs) because of the large I_m and regular spiking due to the after–hyperpolarization. In contrast, when the mean V_m is below threshold, i.e. $I_m < V_{thres}/R_m$, spikes are elicited by temporary

fluctuations in V_m due to synaptic bombardment. Such spiking is in the *fluctuation–driven* regime [Gerstner *et al.*, 2014; Kuhn *et al.*, 2004; Roxin *et al.*, 2011; Tiesinga *et al.*, 2000]. The random synaptic fluctuations cause the spiking to be more irregular, which results in a higher coefficient of variation (CV, defined as the standard deviation (σ) divided by the mean of ISIs), than for the mean–driven regime (cf. **Figure 1D–E**). Therefore irregularity is an indicator of the spiking regime. Another indicator of the fluctuation–driven regime is positive skewness of the firing rate distribution (**Figure 1A-B**). These indicators are used to quantify the fraction of the population that is in one versus the other regime.

AUTHOR CONTRIBUTIONS

Conceptualization, Methodology, Investigation, Software, Visualization, P.C.P. and R.W.B.; Formal Analysis P.C.P.; Writing–Original Draft, Funding Acquisition, Supervision, R.W.B.

ACKNOWLEDGEMENTS

Thanks to György Buzsáki, Daniel F. English and Henrik Lindén for reading and commenting on an earlier version of the manuscript. Funded by the Novo Nordisk Foundation (RB), the Danish Council for Independent Research Medical Sciences (RB and PP) and the Dynamical Systems Interdisciplinary Network, University of Copenhagen.

References

Ahmadian, Y., Rubin, D. B., and Miller, K. D. (2013). Analysis of the stabilized supralinear network. *Neural Comput*, **25**, 1994–2037.

Amit, D. J. and Brunel, N. (1997). Model of global spontaneous activity and local structured activity during delay periods in the cerebral cortex. *Cerebral cortex*, **7**(3), 237–52.

Anderson, J. S., Lampl, I., Gillespie, D. C., and Ferster, D. (2000). The contribution of noise to contrast invariance of orientation tuning in cat visual cortex. *Science*, **290**(5498), 1968–1972.

Arber, S. (2012). Motor circuits in action: specification, connectivity, and function. *Neuron*, **74**(6), 975–89.

Bazhenov, M., Timofeev, I., Fröhlich, F., and Sejnowski, T. J. (2008). Cellular and network mechanisms of electrographic seizures. *Drug Discov Today Dis Models*, **5**(1), 45–57.

Bell, A. J., Tsodyks, M. V., Mainen, Z. F., and Sejnowski, T. J. (1995). Balancing of conductances may explain irregularity of cortical spiking. *Proceedings of the 1st joint symposium on neural computation, Salk institute*, **6**(February), 1–5.

Berg, R. W. and Ditlevsen, S. (2013). Synaptic inhibition and excitation estimated via the time constant of membrane potential fluctuations. *J Neurophysiol*, **110**, 1021–1034.

Berg, R. W., Alaburda, A., and Hounsgaard, J. (2007). Balanced inhibition and excitation drive spike activity in spinal half-centers. *Science*, **315**(5810), 390–3.

Berg, R. W., Ditlevsen, S., and Hounsgaard, J. (2008). Intense synaptic activity enhances temporal resolution in spinal motoneurons. *PLoS one*, **3**(9), e3218.

Berkowitz, A., Roberts, A., and Soffe, S. R. (2010). Roles for multifunctional and specialized spinal interneurons during motor pattern generation in tadpoles, zebrafish larvae, and turtles. *Front Behav. Neurosci.*, **4**(June), 36.

Bikoff, J. B., Gabitto, M. I., Rivard, A. F., Drobac, E., Machado, T. A., Miri, A., Brenner-Morton, S., Famojure, E., Diaz, C., Alvarez, F. J., Mentis, G. Z., and Jessell, T. M. (2016). Spinal Inhibitory Interneuron Diversity Delineates Variant Motor Microcircuits. *Cell*, **165**(1), 207–219.

Blanche, T. J., Spacek, M. A., Hetke, J. F., and Swindale, N. V. (2005). Polytrodes: high-density silicon electrode arrays for large-scale multiunit recording. *J. Neurophysiol.*, **93**(5), 2987–3000.

Britz, O., Zhang, J., Grossmann, K. S., Dyck, J., Kim, J. C., Dymecki, S., Gosgnach, S., and Goulding, M. (2015). A genetically defined asymmetry underlies the inhibitory control of flexor-extensor locomotor movements. *eLife*, **4**(e04718), 1–22.

Brocard, F., Tazerart, S., and Vinay, L. (2010). Do pacemakers drive the central pattern generator for locomotion in mammals? *Neuroscientist*, **16**(2), 139–55.

Brunel, N. (2000). Dynamics of networks of randomly connected excitatory and inhibitory spiking neurons. *J Physiol Paris*, **94**(5-6), 445–63.

Bruno, A. M., Frost, W. N., and Humphries, M. D. (2015). Modular deconstruction reveals the dynamical and physical building blocks of a locomotion motor program. *Neuron*, **86**(1), 304–318.

Buzsáki, G. and Mizuseki, K. (2014). The log-dynamic brain: how skewed distributions affect network operations. *Nat Rev Neurosci*, (February), 1–15.

Destexhe, A., Rudolph, M., and Paré, D. (2003). The high-conductance state of neocortical neurons in vivo. *Nat Rev Neurosci*, **4**(9), 739–51.

Dichter, M. A. and Ayala, G. F. (1987). Cellular mechanisms of epilepsy: a status report. *Science*, **237**(4811), 157–64.

Feldman, J. L., Del Negro, C. A., and Gray, P. A. (2013). Understanding the Rhythm of Breathing: So Near, Yet So Far. *Annu Rev Physiol*, **75**, 423–52.

Feng, J. F. and Brown, D. (1999). Coefficient of variation of interspike intervals greater than 0.5. How and when? *Biol Cybern*, **80**(5), 291–7.

Galarreta, M. and Hestrin, S. (1998). Frequency-dependent synaptic depression and the balance of excitation and inhibition in the neocortex. *Nat Neurosci*, **1**(7), 587–594.

Gerstein, G. L. and Mandelbrot, B. (1964). Random Walk Models for the Spike Activity of a Single Neuron. *Biophys J*, **4**(c), 41–68.

Gerstner, W., Kistler, W. M., Naud, R., and Paninski, L. (2014). *Neuronal Dynamics: From Single Neurons to Networks and Models of Cognition*. Cambridge University Press, New York, NY, USA.

Goulding, M. (2009). Circuits controlling vertebrate locomotion: moving in a new direction. *Nat Rev Neurosci*, **10**(7), 507–18.

Grigonis, R., Guzulaitis, R., Buisas, R., and Alaburda, A. (2016). The influence of increased membrane conductance on response properties of spinal motoneurons. *Brain Res*, **1648**, 110–118.

Grillner, S. (2006). Biological pattern generation: the cellular and computational logic of networks in motion. *Neuron*, **52**(5), 751–66.

Hansel, D. and Mato, G. (2001). Existence and Stability of Persistent States in Large Neuronal Networks. *Phys Rev Lett*, **86**(18), 4175–4178.

Hansel, D. and van Vreeswijk, C. (2002). How noise contributes to contrast invariance of orientation tuning in cat visual cortex. *J Neurosci*, **22**(12), 5118–28.

Hao, Z., Meier, M., and Berkowitz, A. (2014). Rostral spinal cord segments are sufficient to generate a rhythm for both locomotion and scratching but affect their hip extensor phases differently. *J Neurophysiol*, **112**(1), 147–155.

Harris, K. D., Hirase, H., Leinekugel, X., Henze, D. A., and Buzsáki, G. (2001). Temporal interaction between single spikes and complex spike bursts in hippocampal pyramidal cells. *Neuron*, **32**(1), 141–149.

Hennequin, G., Vogels, T. P., and Gerstner, W. (2014). Optimal control of transient dynamics in balanced networks supports generation of complex movements. *Neuron*, **82**(6), 1394–1406.

Higley, M. J. and Contreras, D. (2006). Balanced excitation and inhibition determine spike timing during frequency adaptation. *J. Neurosci.*, **26**(2), 448–57.

Holt, G. R., Softky, W. R., Koch, C., and Douglas, R. J. (1996). Comparison of discharge variability in vitro and in vivo in cat visual cortex neurons. *J Neurophysiol*, **75**(5), 1806–1814.

Hromádka, T., DeWeese, M. R., and Zador, A. M. (2008). Sparse representation of sounds in the unanesthetized auditory cortex. *PLoS Biology*, **6**(1), 0124–0137.

Huckstepp, R. T., Henderson, L. E., Cardoza, K. P., and Feldman, J. L. (2016). Interactions between respiratory oscillators in adult rats. *eLife*, **5**(e14203), 1–22.

Ikegaya, Y., Sasaki, T., Ishikawa, D., Honma, N., Tao, K., Takahashi, N., Minamisawa, G., Ujita, S., and Matsuki, N. (2013). Interpyramid spike transmission stabilizes the sparseness of recurrent network activity. *Cereb Cortex*, **23**(2), 293–304.

Jahn, P., Berg, R. W., Hounsgaard, J., and Ditlevsen, S. (2011). Motoneuron membrane potentials follow a time inhomogeneous jump diffusion process. *J Comput Neurosci*, **31**(3), 563–79.

Jessell, T. M. (2000). Neuronal specification in the spinal cord: inductive signals and transcriptional codes. *Nat Rev Genet*, **1**(1), 20–9.

Kadir, S. N., Goodman, D. F. M., and Harris, K. D. (2014). High-dimensional cluster analysis with the masked EM algorithm. *Neural Comput*, **26**(11), 2379–94.

Keifer, J. and Stein, P. S. (1983). In vitro motor program for the rostral scratch reflex generated by the turtle spinal cord. *Brain research*, **266**(1), 148–51.

Kernell, D. (2006). *The motoneurone and its muscle fibres*. Oxford University Press, New York.

Kiehn, O. (2006). Locomotor circuits in the mammalian spinal cord. *Annu Rev Neurosci*, **29**, 279–306.

Kishore, S., Bagnall, M. W., and McLean, D. L. (2014). Systematic shifts in the balance of excitation and inhibition coordinate the activity of axial motor pools at different speeds of locomotion. *J Neurosci*, **34**(42), 14046–54.

Kleinfeld, D. and Sompolinsky, H. (1988). Associative neural network model for the generation of temporal patterns. Theory and application to central pattern generators. *Biophys J*, **54**, 1039–1051.

Kolind, J., Hounsgaard, J., and Berg, R. W. (2012). Opposing effects of intrinsic conductance and correlated synaptic input on Vm-fluctuations during network activity. *Front. Comput. Neurosci.*, **6**, 40.

Koulakov, A. A., Hromádka, T., and Zador, A. M. (2009). Correlated connectivity and the distribution of firing rates in the neocortex. *J Neurosci*, **29**(12), 3685–94.

Kudina, L. P. (1999). Analysis of firing behaviour of human motoneurones within 'subprimary range'. In *J Physiol Paris*, volume 93, pages 115–123.

Kuhn, A., Aertsen, A., and Rotter, S. (2004). Neuronal integration of synaptic input in the fluctuation-driven regime. *J. Neurosci.*, **24**(10), 2345–56.

Kumar, A., Schrader, S., Aertsen, A., and Rotter, S. (2008). The high-conductance state of cortical networks. *Neural Comput*, **20**(1), 1–43.

Llinas, R. R. (2014). Intrinsic electrical properties of mammalian neurons and CNS function: a historical perspective. *Front. Cell. Neurosci.*, **8**, 320.

Manolakis, D. (1996). Efficient solution and performance analysis of 3-D position estimation by trilateration. *IEEE Trans Aerosp Electron Syst*, **32**(4), 1239–1248.

Manuel, M. and Heckman, C. J. (2011). Adult Mouse Motor Units Develop Almost All of Their Force in the Subprimary Range: A New All-or-None Strategy for Force Recruitment? *J Neurosci*, **31**(42), 15188–15194.

Matthews, P. B. (1996). Relationship of firing intervals of human motor units to the trajectory of post-spike after-hyperpolarization and synaptic noise. *J Physiol*, **492 (Pt 2**(1996), 597–628.

Meehan, C. F., Sukiasyan, N., Zhang, M., Nielsen, J. B., and Hultborn, H. (2010). Intrinsic properties of mouse lumbar motoneurons revealed by intracellular recording in vivo. *J Neurophysiol*, **103**(5), 2599–2610.

Miller, K. D. and Troyer, T. W. (2002). Neural noise can explain expansive, power-law nonlinearities in neural response functions. *J neurophysiol*, **87**(2), 653–9.

Miura, K., Okada, M., and Amari, S.-I. (2006). Estimating spiking irregularities under changing environments. *Neural Comput*, **18**(10), 2359–86.

Mizuseki, K. and Buzsáki, G. (2013). Preconfigured, skewed distribution of firing rates in the hippocampus and entorhinal cortex. *Cell Reports*, **4**(5), 1010–1021.

Mortin, L. I. and Stein, P. S. (1989). Spinal cord segments containing key elements of the central pattern generators for three forms of scratch reflex in the turtle. *J. Neurosci.*, **9**(7), 2285–96.

Mui, J. W., Willis, K. L., Hao, Z. Z., and Berkowitz, A. (2012). Distributions of active spinal cord neurons during swimming and scratching motor patterns. *J Comp Physiol A Neuroethol Sens Neural Behav Physiol*, **198**(12), 877–889.

Murphy, B. K. and Miller, K. D. (2003). Multiplicative gain changes are induced by excitation or inhibition alone. *J. Neurosci.*, **23**(31), 10040–51.

O'Connor, D. H., Peron, S. P., Huber, D., and Svoboda, K. (2010). Neural activity in barrel cortex underlying vibrissa-based object localization in mice. *Neuron*, **67**(6), 1048–1061.

Okun, M. and Lampl, I. (2008). Instantaneous correlation of excitation and inhibition during ongoing and sensory-evoked activities. *Nature neuroscience*, **11**(5), 535–7.

Ostojic, S. (2011). Interspike interval distributions of spiking neurons driven by fluctuating inputs. *J Neurophysiol*, **106**(1), 361–373.

Ozeki, H., Finn, I. M., Schaffer, E. S., Miller, K. D., and Ferster, D. (2009). Inhibitory stabilization of the cortical network underlies visual surround suppression. *Neuron*, **62**(4), 578–92.

Petersen, P. C., Vestergaard, M., Jensen, K. H. R., and Berg, R. W. (2014). Premotor Spinal Network with Balanced Excitation and Inhibition during Motor Patterns Has High Resilience to Structural Division. *J Neurosci*, **34**(8), 2774–2784.

Ponce-Alvarez, A., Kilavik, B. E., and Riehle, A. (2010). Comparison of local measures of spike time irregularity and relating variability to firing rate in motor cortical neurons. *J Comput Neurosci*, **29**(1-2), 351–365.

Powers, R. K. and Binder, M. D. (2000). Relationship between the time course of the afterhyperpolarization and discharge variability in cat spinal motoneurones. *J Physiol*, **528 Pt 1**(2000), 131–50.

Press, W., Teukolsky, S., Vetterling, W., and Flannery, B. (1992). *Numerical Recipes in FORTRAN: The Art of Scientific Computing*. Cambridge University Press.

Priebe, N. J. and Ferster, D. (2005). Direction selectivity of excitation and inhibition in simple cells of the cat primary visual cortex. *Neuron*, **45**(1), 133–45.

Priebe, N. J. and Ferster, D. (2008). Inhibition, spike threshold, and stimulus selectivity in primary visual cortex. *Neuron*, **57**(4), 482–97.

Prut, Y. and Perlmutter, S. I. (2003). Firing properties of spinal interneurons during voluntary movement. I. State-dependent regularity of firing. *J Neurosci*, **23**(29), 9600–10.

Quiroga, R. Q., Nadasdy, Z., and Ben-Shaul, Y. (2004). Unsupervised spike detection and sorting with wavelets and superparamagnetic clustering. *Neural Comput*, **16**(8), 1661–1687.

Renart, A., Moreno-Bote, R., Wang, X.-J., and Parga, N. (2007). Mean-driven and fluctuation-driven persistent activity in recurrent networks. *Neural Comput*, **19**(1), 1–46.

Roxin, A., Brunel, N., Hansel, D., Mongillo, G., and van Vreeswijk, C. (2011). On the distribution of firing rates in networks of cortical neurons. *J Neurosci*, **31**(45), 16217–26.

Rubin, D. B., Hooser, S. D. V., and Miller, K. D. (2015). The stabilized supralinear network : A unifying circuit motif underlying multi-input integration in sensory cortex. *Neuron*, **85**, 402–417.

Salinas, E. and Sejnowski, T. J. (2000). Impact of correlated synaptic input on output firing rate and variability in simple neuronal models. *J Neurosci*, **20**(16), 6193–6209.

Schmitzer-Torbert, N. and Redish, A. D. (2004). Neuronal activity in the rodent dorsal striatum in sequential navigation: separation of spatial and reward responses on the multiple T task. *J Neurophysiol*, **91**(5), 2259–2272.

Sekerli, M., Del Negro, C. A., Lee, R. H., and Butera, R. J. (2004). Estimating action potential thresholds from neuronal time-series: New metrics and evaluation of methodologies. *IEEE Trans Biomed Eng*, **51**(9), 1665–1672.

Shadlen, M. N. and Newsome, W. T. (1994). Noise, neural codes and cortical organization. *Curr Opin Neurobiol*, **4**(4), 569–79.

Shadlen, M. N. and Newsome, W. T. (1998). The variable discharge of cortical neurons: implications for connectivity, computation, and information coding. *J. Neurosci.*, **18**(10), 3870–96.

Shimazaki, H. and Shinomoto, S. (2010). Kernel bandwidth optimization in spike rate estimation. *J. comput. neurosci.*, **29**(1-2), 171–82.

Shimokawa, T. and Shinomoto, S. (2009). Estimating instantaneous irregularity of neuronal firing. *Neural Comput*, **21**(7), 1931–1951.

Shinomoto, S., Kim, H., Shimokawa, T., Matsuno, N., Funahashi, S., Shima, K., Fujita, I., Tamura, H., Doi, T., Kawano, K., Inaba, N., Fukushima, K., Kurkin, S., Kurata, K., Taira, M., Tsutsui, K.-I., Komatsu, H., Ogawa, T., Koida, K., Tanji, J., and Toyama, K. (2009). Relating Neuronal Firing Patterns to Functional Differentiation of Cerebral Cortex. *PLoS Comput Biol*, **5**(7), e1000433.

Shu, Y., Hasenstaub, A., and Mccormick, D. A. (2003). Turning on and off recurrent balanced cortical activity. *Nature*, **423**(May), 288–293.

Silver, R. A. (2010). Neuronal arithmetic. *Nat Rev Neurosci*, **11**(7), 474–89.

Softky, W. R. and Koch, C. (1993). The highly irregular firing of cortical cells is inconsistent with temporal integration of random EPSPs. *J. Neurosci.*, **13**(1), 334–50.

Song, S., Sjostrom, P. J., Reigl, M., Nelson, S., and Chklovskii, D. B. (2005). Highly nonrandom features of synaptic connectivity in local cortical circuits. *PLoS Biol*, **3**(3), e68.

Stein, P. (2005). Neuronal control of turtle hindlimb motor rhythms. *J Comp Physiol A Neuroethol Sens Neural Behav Physiol*, **191**, 213–229.

Stern, E. A., Kincaid, A. E., and Wilson, C. J. (1997). Spontaneous subthreshold membrane potential fluctuations and action potential variability of rat corticostriatal and striatal neurons in vivo. *J Neurophysiol*, **77**(4), 1697–715.

Stevens, C. F. and Zador, a. M. (1998). Input synchrony and the irregular firing of cortical neurons. *Nat Neurosci*, **1**(3), 210–7.

Takekawa, T., Isomura, Y., and Fukai, T. (2012). Spike sorting of heterogeneous neuron types by multimodality-weighted PCA and explicit robust variational Bayes. *Front Neuroinform*, **6**(5), 1–13.

Tiesinga, P. H. E., José, J. V., and Sejnowski, T. J. (2000). Comparison of current-driven and conductance-driven neocortical model neurons with Hodgkin-Huxley voltage-gated channels. *Phys Rev E*, **62**(6), 8413–8419.

van Vreeswijk, C. and Sompolinsky, H. (1996). Chaos in neuronal networks with balanced excitatory and inhibitory activity. *Science*, **274**(5293), 1724–6.

van Vreeswijk, C. and Sompolinsky, H. (1998). Chaotic balanced state in a model of cortical circuits. *Neural Comput*, **10**(6), 1321–1371.

Vandecasteele, M., Deniau, J. M., and Venance, L. (2011). Spike frequency adaptation is developmentally regulated in substantia nigra pars compacta dopaminergic neurons. *Neuroscience*, **192**, 1–10.

Vestergaard, M. and Berg, R. W. (2015). Divisive Gain Modulation of Motoneurons by Inhibition Optimizes Muscular Control. *J Neurosci*, **35**(8), 3711–3723.

Vogels, T. P., Rajan, K., and Abbott, L. F. (2005). Neural network dynamics. *Annu Rev Neurosci*, **28**(March), 357–76.

Walloe, S., Nissen, U. V., Berg, R. W., Hounsgaard, J., and Pakkenberg, B. (2011). Stereological estimate of the total number of neurons in spinal segment D9 of the red-eared turtle. *J. Neurosci.*, **31**(7), 2431–5.

Wehr, M. and Zador, A. M. (2003). Balanced inhibition underlies tuning and sharpens spike timing in auditory cortex. *Nature*, **426**(6965), 442–6.

Wohrer, A., Humphries, M. D., and Machens, C. K. (2013). Population-wide distributions of neural activity during perceptual decision-making. *Prog Neurobiol*, **103**, 156–193.

Young, E. D., Robert, J. M., and Shofner, W. P. (1988). Regularity and latency of units in ventral cochlear nucleus: implications for unit classification and generation of response properties. *J Neurophysiol*, **60**(1), 1–29.

Yuste, R. (2015). From the neuron doctrine to neural networks. *Nat Rev Neurosci*, **16**(8), 487–497.

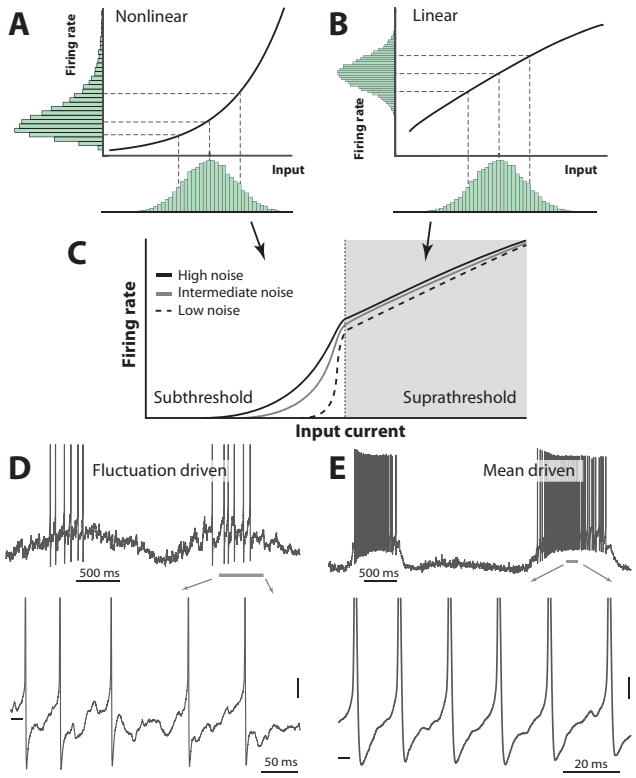

Figure 1: Skewness of the rate distribution reveals two regimes of neuronal spiking. (**A**) In the fluctuation–driven regime the mean input is below the spiking threshold and the IO-curve has a nonlinear shape. A normally distributed input current (shown below x–axis) is transformed into a skewed firing rate distribution (y-axis). (**B**) In contrast, if the mean input is above threshold, the transformation is linear and the firing rate distribution is symmetric. (**C**) IO–function for both regimes: Linear for suprathreshold region and nonlinear for subthreshold region. The noise level affects the curvature of the nonlinearity (3 curves illustrate different levels of noise). (**D**) Sample recordings during motor activity from two spinal neurons in the subthreshold region, where the spiking is irregular and driven by fluctuations, and the supra–threshold region (**E**), where the mean input is above threshold and spiking is regular. Highlighted area shown at bottom. Spikes in bottom panel are clipped. Tick marks: -50 mV, scale bars: 5 mV. (A–B) adapted from [Roxin *et al.*, 2011].

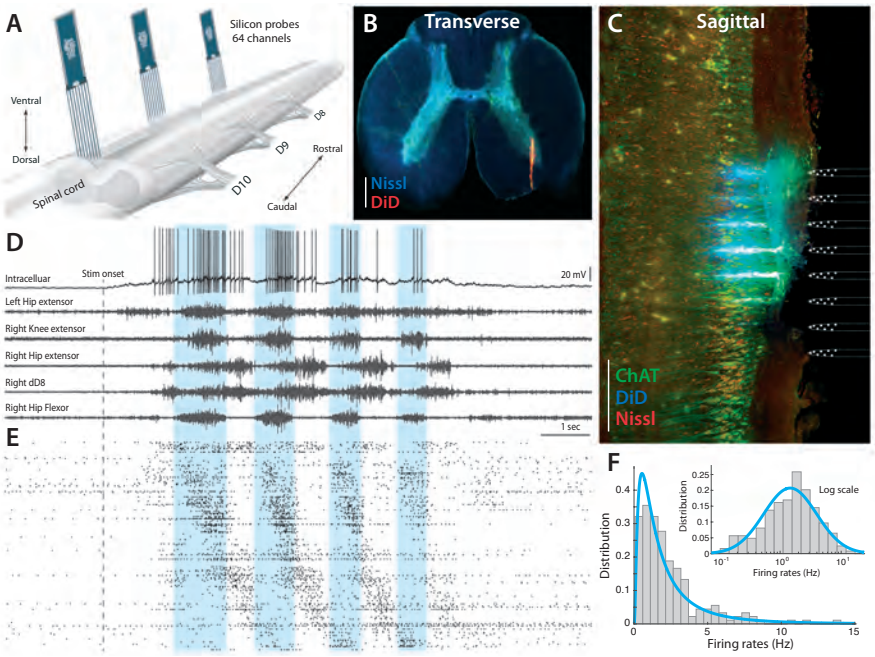

Figure 2: Parallel neuronal activity in the lumbar enlargement during rhythmic motor activity. (**A**) Illustration of experiment with three silicon probes inserted into the lumbar spinal cord of a turtle. Histological verification: transverse (**B**) and sagittal (**C**) slices, 200μm thick, showing the location of the silicon probes in the spinal cord (red traces and location illustrated on right, electrodes stained with DiD). ChAT staining in green and Nissl stain in blue. Scale bars: 500 μm (**D**) V_m of a single neuron (top) concurrently recorded with five motor nerves (traces below) during scratching behavior induced by a somatic touch (onset indicated, 10-s duration). (**E**) Rastergram showing the parallel-recorded single units (∼200 neurons) sorted according to hip flexor phase. (**F**) Firing rate distribution is positively skewed and normally distributed on a log–scale, i.e. lognormal (inset). V_m resting level in (D) is -60 mV. For details, see Figure supplement 1 and 2.

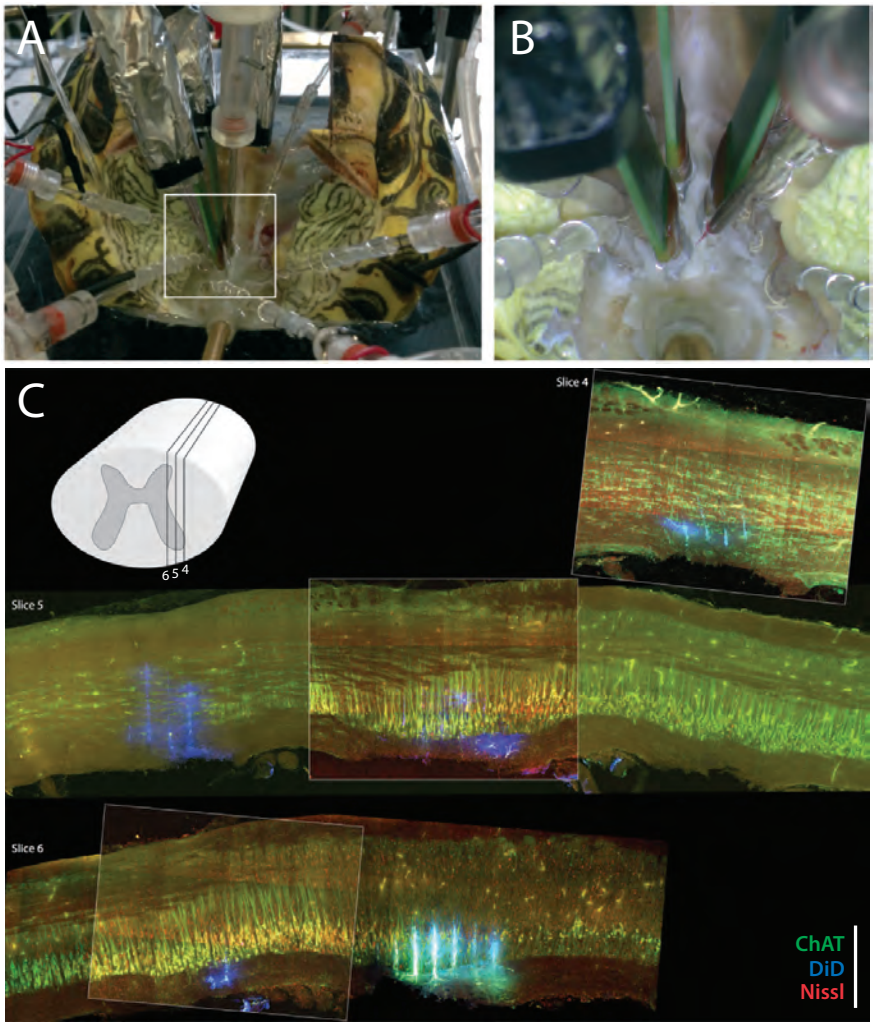

figure supplement 1: Experimental setup. (**A**) Preparation with electrodes inserted into the spinal cord of a turtle, which is lying on its back with the caudal part of the carapace and spinal cord intact. The scratch reflex motor pattern is activated by the mechanical touch of the carapace with a rod attached to an actuator. (**B**) Close–up from (**A**) with nerve suction electrodes (with silver wires), an intracellular electrodes and the 3 silicon probes (green) inserted into the spinal cord. (**C**) *Post–hoc* histological reconstruction of the location of three Berg64–probes. The tissue is immunostained for ChAT-positive motoneurons (green) and Nisslstained neurons (red) to differentiate motoneurons from interneurons. The probes were painted with DiI prior to insertion leaving a fluorescent trace (blue), although unspecific ChAT staining at the shank location gives a cyan appearance in slice 6. Inset illustration indicates parasagittal locations of slice 4, 5 and 6. Scale bar: 500 μm

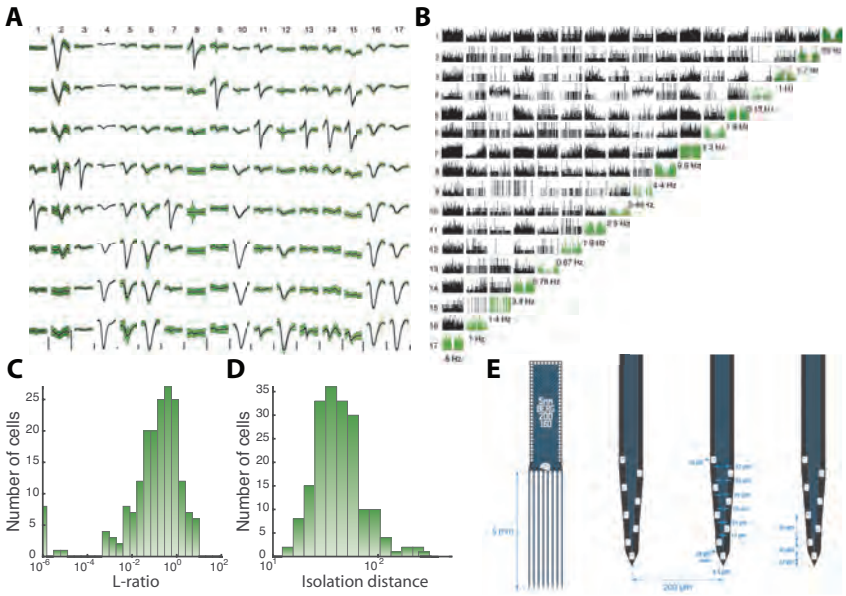

figure supplement 2: Sorted sample units, quality measures, and probe layout. (**A**) Average waveforms (black) and ±SD (green) of 17 units (columns) recorded by 8 electrodes (rows) situation on the same shank of a Berg64–probe. Vertical scale bar 100μV. (**B**) Correlogram matrix for the same 17 units with the autocorrelograms in diagonal (green). The quality of the spike sorting is verified by the *L-ratio* (**C**) and *Isolation distance* (**D**) for all units from the same session. (**E**) The Berg64–probe (Neuronexus inc) consists of 8 shanks with 8 electrodes on each shanks, located at the edge to sample over the largest volume of tissue. Dimensions are indicated.

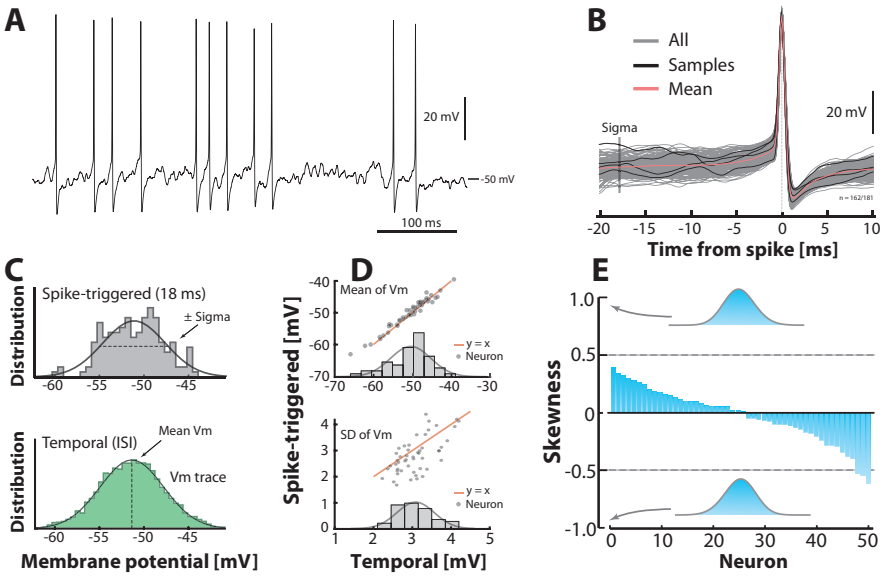

Figure 3: Subthreshold V_m–distributions are symmetric. (**A**) Sample cell spiking in the fluctuation–driven regime, and (**B**) its spike–triggered overlay to determine the V_m–distribution of trajectories 18 ms prior to spike–onset ('sigma'). (**C**) The V_m–distribution is estimated in two ways: via samples of V_m–instances prior to the spike peak (top, vertical line 'sigma' in **B**) and over time via the interspike intervals (bottom). (**D**) Mean temporal– vs. spike–triggered–estimates (top) are closely related (orange unity–line) and have a near normal distribution of means (inset). For details, see Figure supplement 1 and 2. Similarly, the variability of the two estimates (SD) are closely related (bottom). (**E**) Sorted skewness for all neurons in fluctuation–driven regime indicate symmetric V_m–distributions (temporal). Inset distributions with skewness of ± 1 illustrate no discernible asymmetry. The extreme skewness observed in the data set is around ± 0.5 (broken lines).

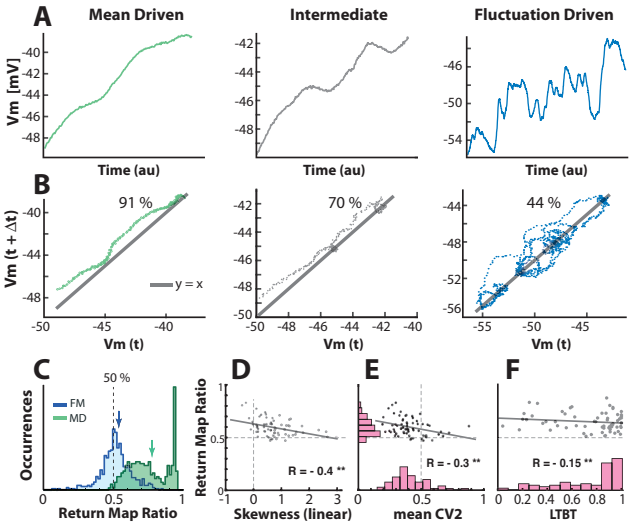

figure supplement 1: Quantifying the degree of fluctuations and selecting neurons in fluctuation–driven regime using the return map ratio metric. (**A**) The inter–spike V_m–trajectory of three sample neurons in mean–driven (left), intermediate (middle) and fluctuation–driven spiking regime (right). In the mean–driven regime the inter–spike trajectory moves directly from AHP resetting towards threshold, whereas in the fluctuation–driven regime the trajectory is convoluted and indirect (right). (**B**) The degree of convolution in the trajectory can be quantified using *return mapping*, i.e. plotting $V_m(t)$ versus $V_m(t + \Delta t)$, and quantifying the fraction of points above versus below the unity-line ($y = x$), which we refer to as the *return map ratio*. An even ratio close to 0.5 represents convoluted path (right), whereas a uneven ratio (close to 1) represent a direct path (left). Ratios are indicated in %. (**C**) The distribution of return map ratios for all ISIs, shown for two sample neurons, one having distribution mean close to 0.5, i.e. a fluctuation–driven regime and one having the mean close to 0.8, i.e. in the mean–driven regime (blue and green arrows). The mean return map ratio of all neurons ($n = 68$) has a significant anti–correlation with skewness of firing rate distribution (**D**), spike irregularity (CV_2) (**E**), as well as the least time spent below threshold (LTBT) of V_m (**F**).

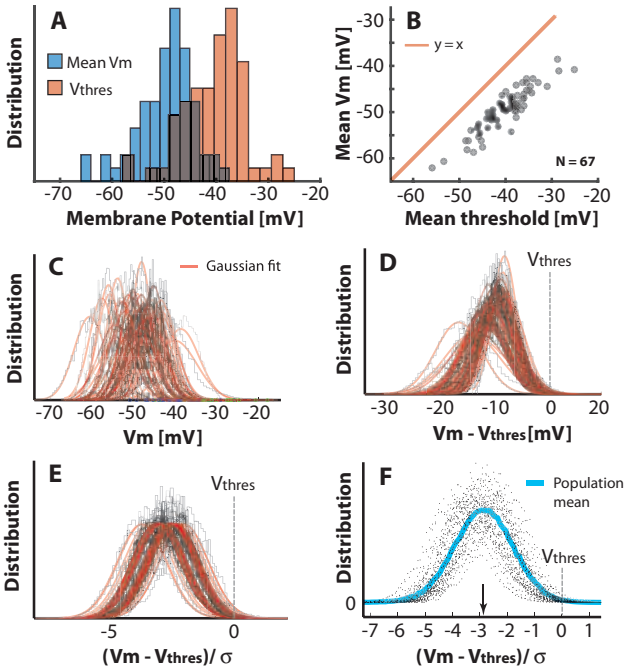

figure supplement 2: Population–distribution of mean V_m is Gaussian. (**A**) The mean V_m for the population of neurons is symmetrically near Gaussian–distributed (blue). The mean threshold for the same population is depolarized (red). (**B**) The mean thresholds correlate with the values of mean V_m and the thresholds are more depolarized as indicated by a rightward shift compared with the unity line (red). (**C**) Scatter plot of all the histograms of V_m with Gaussian fits (red). (**D**) Histogram of the V_m distributions with the individual mean thresholds (V_{thres}) subtracted (broken line indicates the relative location of V_{thres}). Note that the V_m distributions, which have their mean far from threshold, also have a larger SD. (**E**) Normalizing each distribution with SD (σ) to assess the distance in terms of the size of fluctuations, i.e. $(V_m - V_{thres})/\sigma$. (**F**) Scatter plot of all the distributions of $(V_m - V_{thres})/\sigma$, has a near Gaussian distribution as indicated with the sliding population mean (blue). The mean distance to threshold is approximately 3σ (arrow).

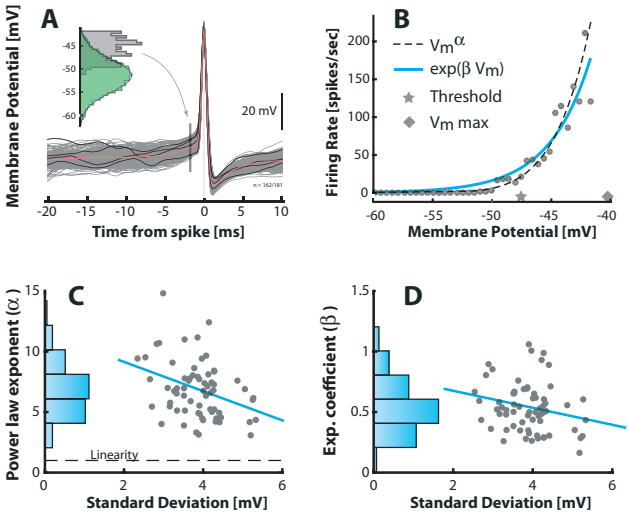

Figure 4: Subthreshold spike–response curve is supralinear and depends on V_m–fluctuations. (**A**) A spike–triggered overlay to determine the V_m–distribution of trajectories prior to spike–onset (gray histogram, 1.7 ms prior to peak) to compare with the total (temporal) V_m–distribution (green histogram). (**B**) The firing rate versus V_m in subthreshold region for a sample neuron is strongly nonlinear. A power–law (broken line) and an exponential (blue line) are fitted to capture the nonlinearity. Note that the mean threshold ($\star$) is below the largest subthreshold fluctuation ($\diamond$), likely due to a depolarization of threshold associated with a higher firing rate (see also Figure 6 supplement 1). (**C**) Power–law exponent (α) for different neurons are weakly anti–correlated with the fluctuations (SD) in their V_m ('sigma', Figure 3B, $R = -0.34$, $p < 0.01$). Linearity is indicated by horizontal broken line. (**D**) Exponential coefficient (β) for different neurons are also anti–correlated with the fluctuations in V_m albeit not significantly ($R = -0.22$, $p > 0.05$).

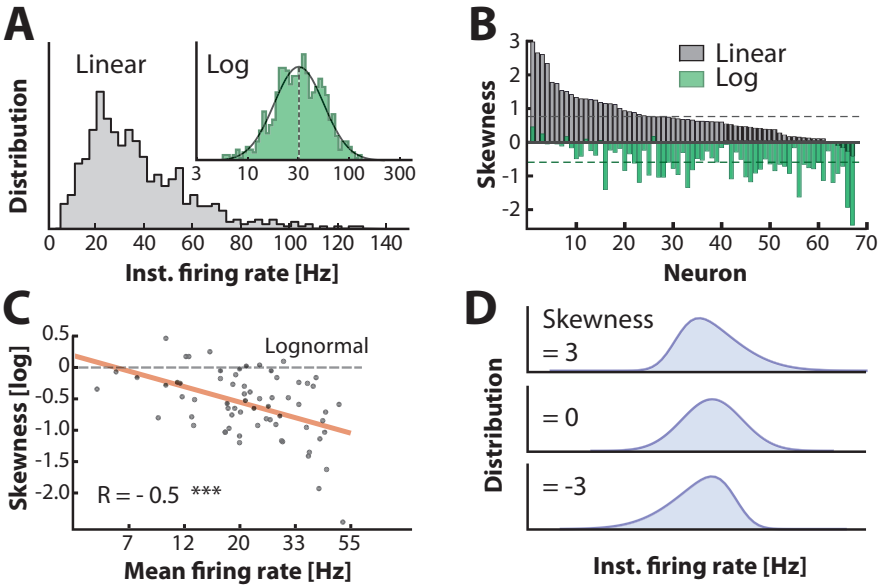

Figure 5: Firing rate distributions are skewed to a variable degree depending on mean firing rate. (**A**) Distribution of instantaneous firing rates for a sample neuron is positively skewed on a linear axis and lognormal–like (green histogram, inset). Mean indicated by broken vertical line. (**B**) Sorted distribution skewness on linear (gray) and logarithmic axes (green) for each neuron in the population. (**C**) The log–skewness across neurons is negatively correlated ($R = -0.5$, $p < 0.001$) with mean firing rate, which indicates that higher firing rates are found in the mean–driven regime and less lognormally–distributed, i.e. departing from broken line. (**D**) Illustration of firing rate distributions that have positive skewness (top), zero skewness (Gaussian, middle) and negative skewness (bottom) representing the range observed in the data (**B**).

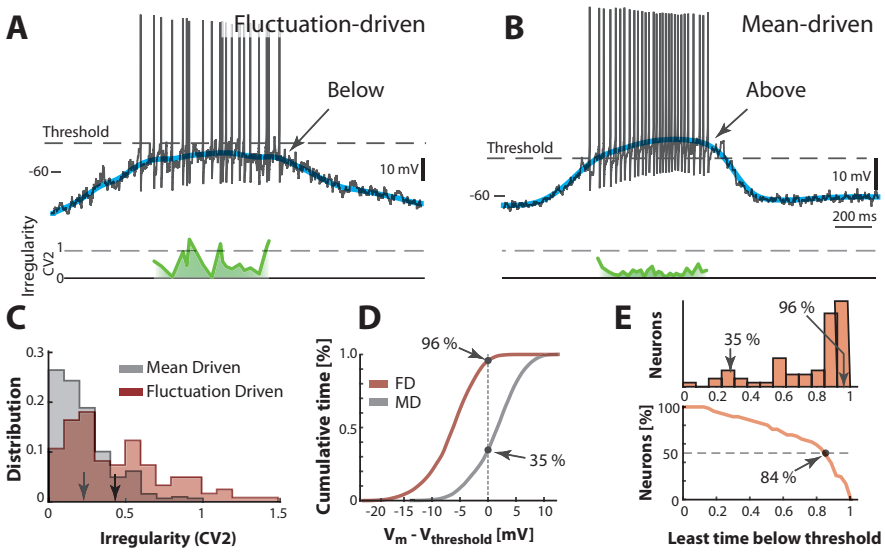

Figure 6: Two contrasting sample neurons found in the two regimes. (**A**) Sample neuron in fluctuation–driven regime, where the mean V_m (blue line) is below lowest threshold (broken line), the spikes are irregular ($CV_2 \approx 0.5$–1, green line) and driven by fluctuations (arrow). (**B**) Second sample cell found in mean–driven regime, where the mean V_m is above threshold during the cycle (arrow). The spiking is more regular, i.e. low CV_2 (green line). (**C**) Mean–driven neuron (gray) has lower CV_2 than the fluctuation–driven neuron (brown). Means indicated (arrows). (**D**) Cumulative time of V_m shows the fluctuation–driven neuron (FD) spends more time below threshold (96%) than the mean–driven (MD, 35%). (**E**) Top: Time below threshold for population of neurons (cells from A–D indicated). Bottom: Least time spent below threshold versus a given fraction of neurons (reverse cumulative distribution function). Half of the neurons (broken line) spend at least 84% of the time in fluctuation–driven regime, i.e. have V_m below threshold.

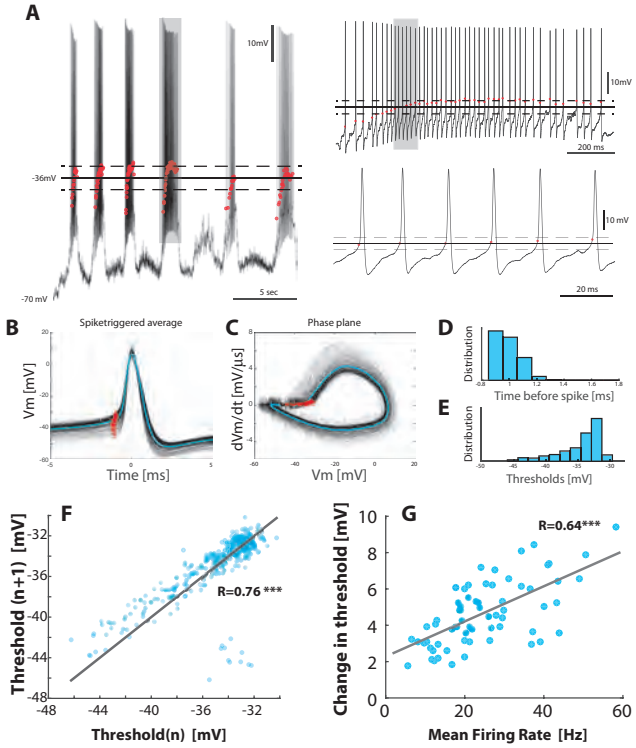

figure supplement 1: Threshold depolarizes with increase in firing rate. (**A**) Sample recording with the threshold (red dots) for each spike (left). Mean threshold (solid line) ± SD (broken lines). Right top: the selected cycle from trace in left (fourth cycle indicated by gray horizontal bar at top). Right bottom: Selected region on shorter timescale (gray rectangle from top trace). (**B**) Spike–triggered overlay with the thresholds indicated (red dots). (**C**) Detection of threshold via method by Sekerli *et al.* [2004]: Threshold is found at the maximum of the second derivative of the trajectory in phase plane plot of V_m versus dV_m/dt (red dots). (**D**) Distribution of threshold location prior to spike peak. (**E**) Distribution of threshold values in V_m. (**F**) Return map of the spike threshold values, shows a strong correlation between neighboring threshold values (n vs. $n+1$). (**G**) The change in threshold, $V_{thresh} - V_{thres,Q5}$, with mean firing rate, where $V_{thres,Q5}$ is the threshold at the 5% quantile and V_{thresh} is the threshold for individual spikes.

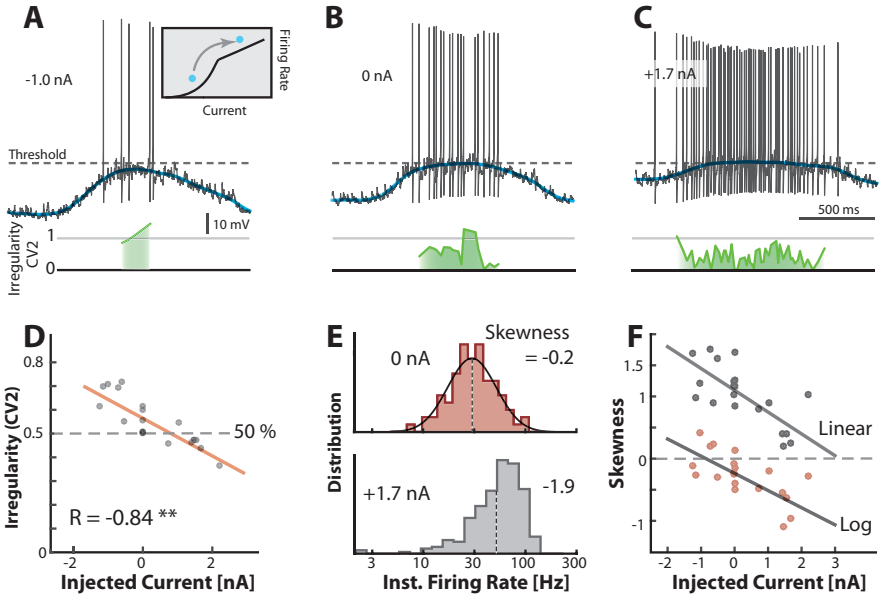

Figure 7: Transition between regimes can be induced by injected current. (**A**) Hyperpolarizing V_m of a sample neuron during the motor cycle with negative injected current (-1.0 nA). Negative current hyperpolarizes mean V_m (blue) and increases irregularity ($CV_2 \approx 1$, green line) compared with control condition (**B**). (**C**) Positive current injection (1.7nA) has the opposite effect: Depolarization, more regular spiking and higher firing rate. (**D**) Mean of CV_2 over a trial vs. the constant injected current for that trial has negative correlation. (**E**) Firing rate is lognormally distributed in control (top), but negatively skewed (skewness = -1.9) when added current increases mean–driven spiking (bottom). (**F**) Skewness of firing rate distribution is negatively correlated with injected current. Linear skewness shown in top gray points ($R = -0.73$, $p < 0.001$) and log-skewness shown in bottom red points ($R = -0.70$, $p < 0.001$). Same neuron throughout.

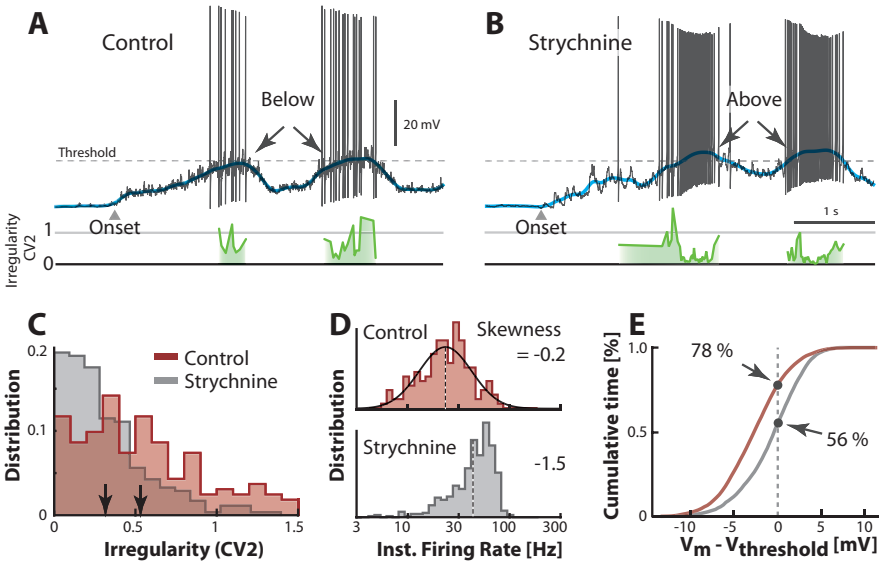

Figure 8: Transition between regimes induced by unbalancing E/I. (**A**) Sample cell in control condition and after reduction of inhibition with local strychnine (**B**). Onset of motor program indicated (△). Blocking inhibition results in a larger net inward current, which drives the mean V_m (blue lines) across threshold to more mean–driven regime. As a result the spiking is less irregular on the peaks as measured with CV_2 (cf. green lines). (**C**) Irregularity (CV_2) was smaller after application of strychnine (arrows indicate mean, histogram truncated at 1.5). (**D**) Firing rate distribution is symmetric on log–scale (top, skewness =-0.2) and negatively skewed when inhibition is blocked (bottom, skewness=-1.5). (**E**) Strychnine induces a more depolarized Vm and a lower cumulative time spend below the threshold (compare 78% with 56%). Same neuron throughout.

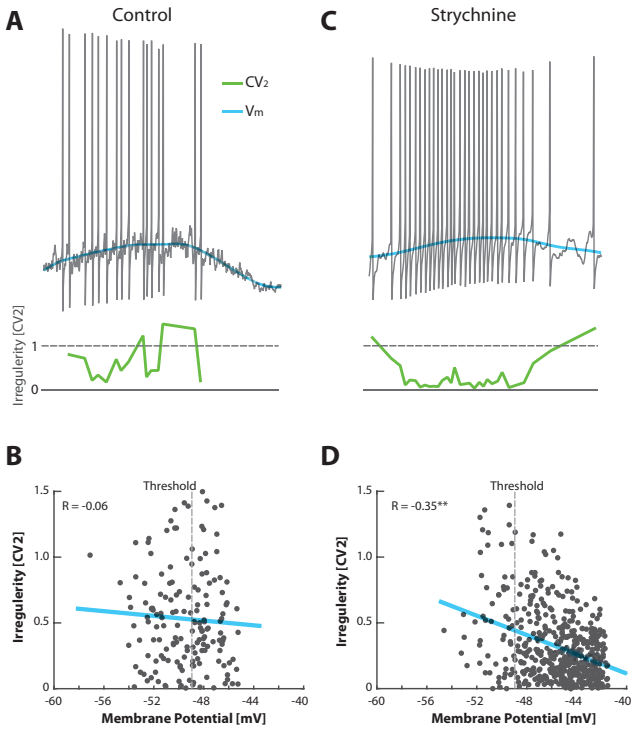

figure supplement 1: Unbalancing E/I induces an anti–correlation between irregularity and depolarization. (**A**) No obvious relationship between mean V_m (blue) and the irregularity of the spike (CV_2, green) in the control condition of a sample cell in the fluctuation–driven regime. (**B**) The fluctuation–driven regime is manifested as a lack of significant correlation between irregularity for each pair of ISIs (CV_2) and the mean V_m ($R = -0.06$, $p = 0.48$). The most negative threshold indicated by vertical broken line. (**C**) Spiking of same cell as in (**A**) after elimination of glycinergic inhibition by local application of strychnine, which causes depolarized in V_m, more regular spiking at higher rate and slower fluctuations in V_m. (**D**) The removal of inhibition also puts the spiking into the mean–driven regime, which is manifested as a significant anti-correlation between irregularity of the spiking and mean V_m ($R = -0.35$, $p \ll 0.0001$).

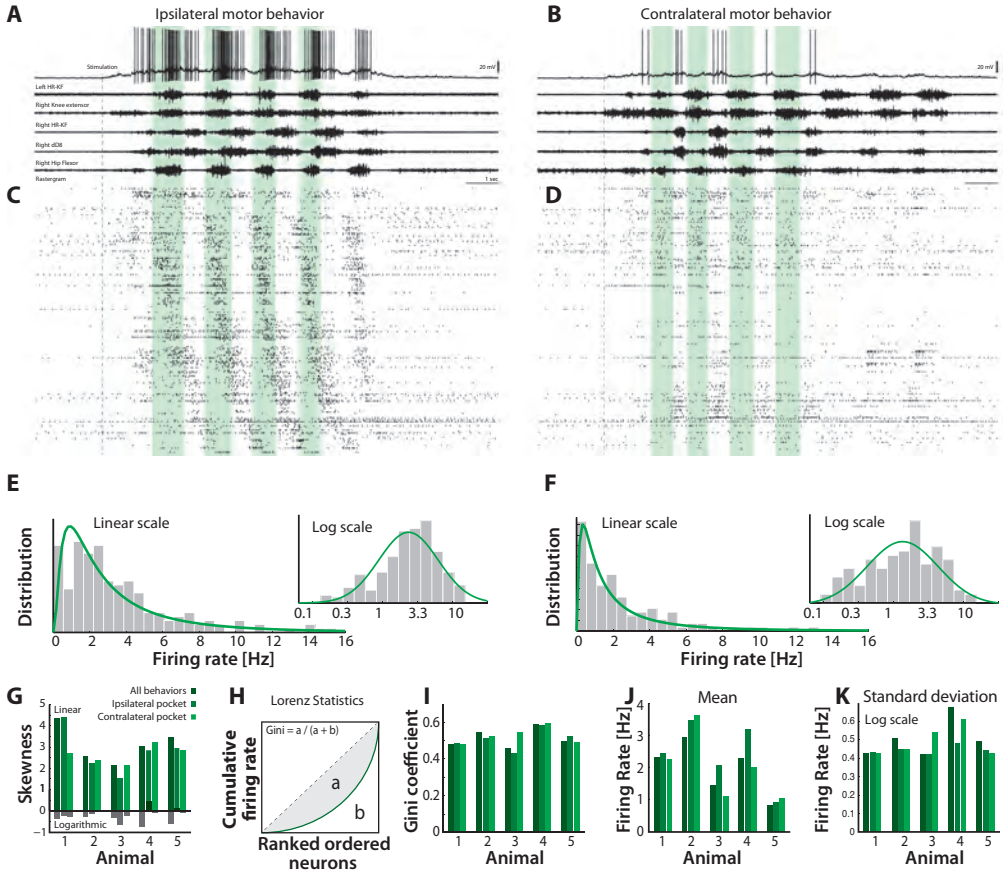

Figure 9: Skewed neuronal participation across behaviors. (**A-B**) Two distinct motor behaviors: Ipsilateral pocket scratch (left panel) and contralateral pocket scratch (right panel) shown by intracellular recordings (top) and motor nerve activities. (**C-D**) Rastergrams showing the unit activities during ipsilateral pocket scratch (**C**) and contralateral pocket scratch (**D**). Green areas mark the hip flexor phase. (**E-F**) spike count firing rate distribution for the behaviors on linear and a semi-log plot (insets), indicate lognormal participation. Lognormal functions are fitted (solid green lines). (**G**) Skewness on logarithmic (green bars) and linear scale (gray bars) is preserved across animals. (**H**) The inequal neuronal participation is calculated using Lorenz curve and gini coefficient. (**I**) Gini–coefficients cluster around 0.5 across behaviors and animals. Mean (**J**) and standard deviation on (**K**) of the distribution of firing rates on log–scale across behaviors and animals. V_m resting level in (A–B) is -60 mV.

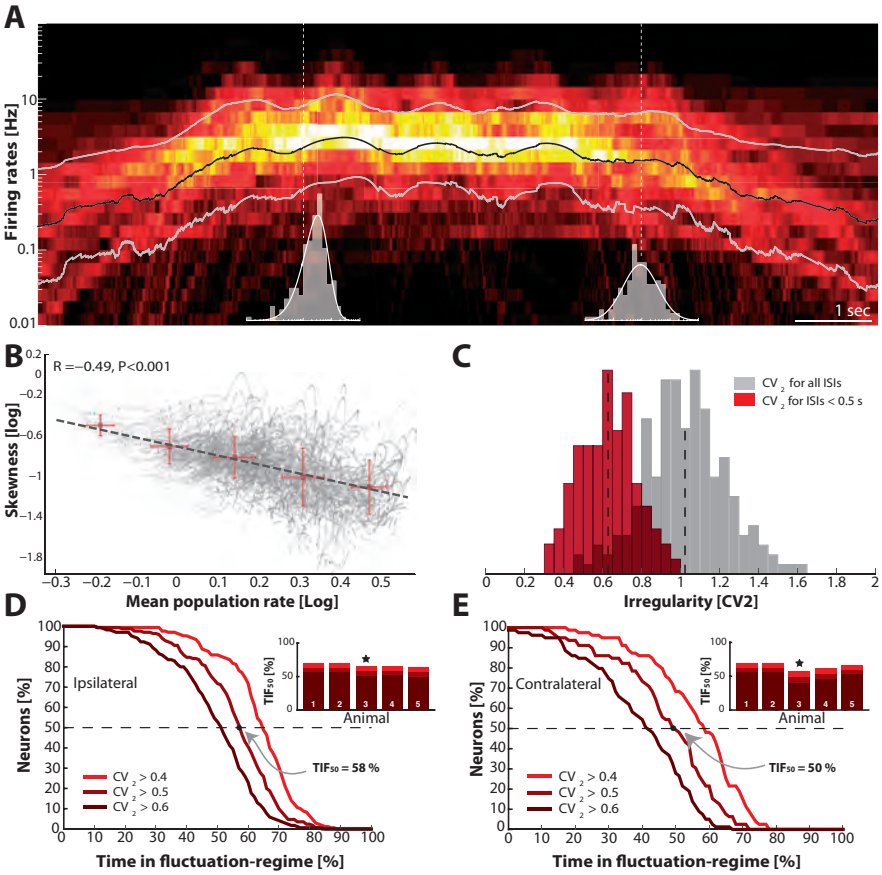

Figure 10: Skewness and irregularity across the neuronal population gauge occupation in both regimes across time. (**A**) Heat map of the distribution of firing rates across the population ($n = 190$ units, 1 animal) on log–scale (y–axis) as a function of time (x–axis). Lognormal mean ± SD are indicated as black and grey lines, respectively. Distribution is indicated (gray histograms) at two different time points (broken vertical lines). (**B**) Lognormal mean population firing rate (black line in A) versus log–skewness are negatively correlated, indicating more neurons move into mean–driven regime as the population rate increases. Scatter due to multiple trials, which is binned in sections, red crosses. (**C**) Distribution of irregularity (mean CV_2) across population for all ISIs (gray) and when excluding of inter–burst intervals (red). (**D**) Fraction of neurons, which spend a given amount of time in fluctuation–driven regime ($i_{crit} = 0.4, 0.5$ and 0.6) normalized to 100% (Reverse cumulative distribution). The least time spent in fluctuation–driven regime by half of the neurons (TIF_{50}) is given by the intercept with the broken horizontal line and distribution (indicated by arrow). For this sample animal and behavior $TIF_{50} = 56\%$. Inset: Values across animals, sample animal indicated ($\star$). (**E**) The TIF_{50}–values across animals in both behaviors as indicated by similarity in values are remarkably conserved.

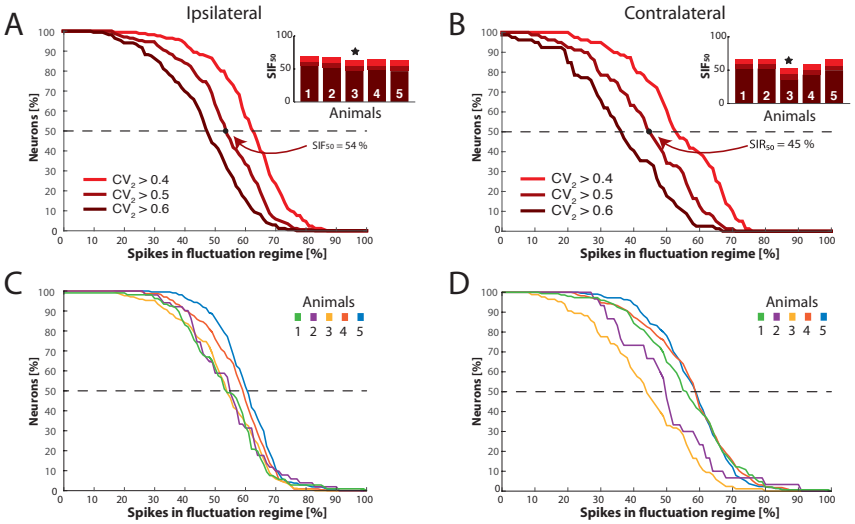

figure supplement 1: Distribution of neurons having fluctuation driven spikes and SIF_{50} values. (**A**) Reverse cumulative distribution of neurons (y–axis) having a given number of spikes driven by fluctuations (x–axis) for ipsilateral scratching for a sample animal and three values of i_{crit} (0.4, 0.5, and 0.6). The minimal fraction of spikes driven by fluctuation in half of the neuronal population, SIF_{50}, shown in inset. Sample animal indicated ($\star$). (**B**) Same as (**A**) but for contralateral scratching. (**C**) The reverse cumulative distributions similar to (**A**) for all five animals and for $i_{crit} = 0.5$ for ipsilateral scratching and for contralateral scratching (**D**).

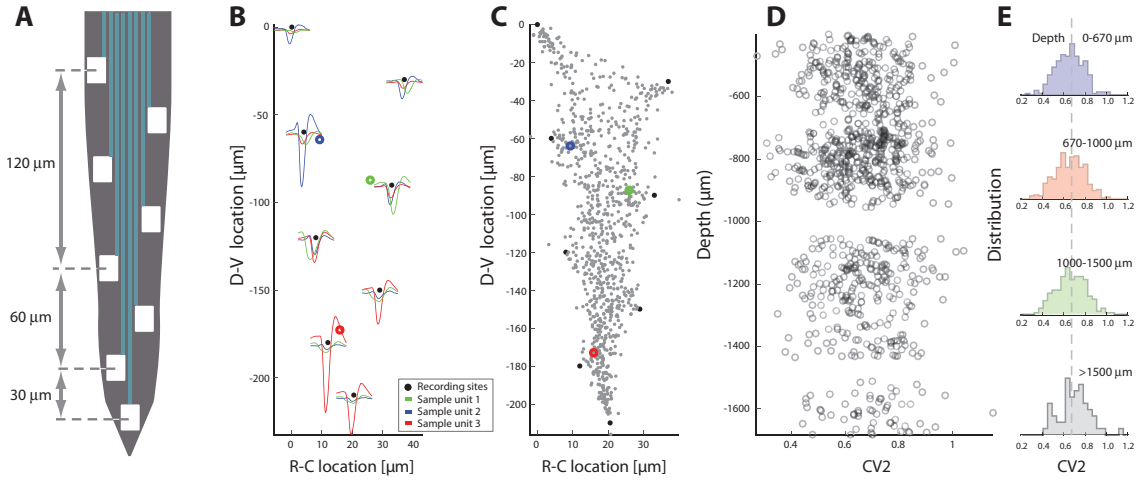

Figure 11: Spiking irregularity is independent of cellular location. (**A**) Layout of the 8 electrodes on a shank, which span a total of 210 μm in the dorsoventral axis. (**B**) Recorded waveforms at different locations of three sample units (colored in red, blue and green). The node locations are estimated via trilateration and indicated as rings. Electrode locations are indicated as black dots. (**C**) Composite of source-locations for all shanks and all animals (total $n = 921$ cells). The location of sample units from B indicated in colors. (**D**) Irregularity of the associated spiking are estimated (mean CV_2 on x-axis) versus the dorsoventral location (y–axis), where the unit locations are corrected for the depth of the individual shank with respect to the spinal cord surface. (**E**) The binned distributions of CV_2 as a function of depth. The distribution means are remarkably similar (broken line as fiducial) and a KS–test indicates no significant difference.